Advances in threshold photoelectron spectroscopy (TPES) and threshold photoelectron photoion coincidence (TPEPICO)

Baer, Tomas; Tuckett, Richard

DOI:
10.1039/C7CP00144D

Document Version
Peer reviewed version

Citation for published version (Harvard):
Baer, T & Tuckett, RP 2017, 'Advances in threshold photoelectron spectroscopy (TPES) and threshold photoelectron photoion coincidence (TPEPICO)', Phys. Chem. Chem. Phys., vol. 19, no. 15, pp. 9698-9723. https://doi.org/10.1039/C7CP00144D

Front Cover of *Phys Chem Chem Phys.*, (2017) 19 (xx) (probably to be published 28 April 2017)

Deity of Science: Award winning original art work by Dr Jonelle Harvey (PhD student of RPT) who is now a Professional Standards Specialist at the Royal Society of Chemistry. It depicts the *i*PEPICO endstation at the Swiss Light Source (where some of the data described in the Perspective article were taken), and the constant stream of information produced from reactions generated from within

DOI: 10.1039/c7cp00144d: ***Image reproduced by permission of Jonelle Harvey, PCCP, (iss), 19, 2017***

Advances in Threshold Photoelectron Spectroscopy (TPES) and Threshold Photoelectron Photoion Coincidence (TPEPICO)

Tomas Baer [a] and Richard P. Tuckett [b] (28.2.17, after proofs returned to PCCP)

a) Chemistry Department, University of North Carolina, Chapel Hill, NC 27599-3290
b) Chemistry Department, University of Birmingham, B15 2TT, UK

Abstract

The history and evolution of molecular threshold photoelectron spectroscopy and threshold photoelectron photoion coincidence spectroscopy (TPEPICO) over the last fifty years are reviewed. Emphasis is placed on instrumentation and the extraction of dynamical information about energy selected ion dissociation, not on the detailed spectroscopy of certain molecules. Three important advances have expanded greatly the power of the technique, and permitted its implementation on modern synchrotron radiation beamlines. The use of velocity focusing of threshold electrons onto an imaging detector in the 1990s simultaneously improved the sensitivity and electron energy resolution, and also facilitated the subtraction of hot electron background in both threshold electron spectroscopy and TPEPICO studies. The development of multi-start multi-stop collection detectors for both electrons and ions in the 2000s permitted the use of the full intensity of modern synchrotron radiation thereby greatly improving the signal-to-noise ratio. Finally, recent developments involving imaging electrons in a range of energies as well as ions onto separate position-sensitive detectors has further improved the collection sensitivity so that low density samples found in a variety of studies can be investigated. As a result, photoelectron photoion coincidence spectroscopy is now well positioned to address a range of challenging problems that include the quantitative determination of compositions of isomer mixtures, the detection and spectroscopy of free radicals produced in pyrolysis or discharge sources as well as in combustion studies.

1. Introduction

Photoelectron spectroscopy (PES) and Threshold photoelectron spectroscopy (TPES) both had their beginnings in the 1960's. In PES, a fixed energy light source is used to ionize a molecule and the ejected electron kinetic energies are generally dispersed with an electrostatic analyzer. On the other hand, in TPES, a tunable light source is used to scan through the various ion states while collecting initially near zero kinetic energy electrons, commonly called threshold electrons . In both cases, the ion electronic and vibrational states are identified by conservation of energy illustrated by the following equation.

$$E_{ion} = h\nu - IE - E_{el} \qquad (1)$$

In this equation, E_{ion} is the ion internal energy relative to its ground state ionization energy (IE), $h\nu$ is the photon energy, and E_{el} is the kinetic energy of the electron. These two approaches differ profoundly in their experimental requirements as well as in the principle used to measure the electron energies. In PES a relatively simple, low pressure, line source such as a He I lamp is used to provide the radiation, while in TPES, a vacuum UV monochromator is used to disperse a continuum light source. True continuum light sources, such as the Ar and He Hopfield continua must operate at ca 0.6 bar in a windowless mode and thus require substantial differential pumping in order to maintain the monochromator at a pressure of $< 10^{-7}$ bar. It is thus reasonable to ask why TPES was pursued at all, when its experimental requirements are so much greater than those required for PES.

One advantage of TPES is its capacity to deliver considerably higher electron energy resolution which is now limited primarily by the resolution of the photon source. But even more important is the advantage threshold electron detection provides when the electrons are collected in coincidence with the ion, thereby making possible the study of energy selected ions. As will become clear, a key requirement in such coincidence studies is the ability to collect both electron and ions with high collection efficiencies. In the case of PES, energetic electrons are ejected in all directions and only those heading toward the electrostatic energy analyzer can be collected. This represents a small fraction which typically does not exceed 0.1 %. On the other hand, threshold electrons can be collected with near 100% collection efficiencies. Secondly, in order to have good energy resolution, the absence of electric fields is essential in PES, which makes ion extraction difficult. In contrast, moderate electric fields were quite compatible with the early TPES methods, and today even high electric fields can be used in electron ion coincidence studies which do not require any compromises for either electron energy resolution, ion mass resolution, nor the collection efficiencies for either particle. The threshold photoelectron photoion coincidence (TPEPICO) experiment has thus largely replaced the earlier PES coincidence (or PEPICO) experiments,[1-3] at least as practiced by chemists on polyatomic systems. On the other hand, there is a notable physics community that continues to investigate mostly di- and triatomic ion dissociations using PEPICO with energetic electrons. This field, which is outside the scope of this review, has recently been reviewed.[4]

Major advances in the past decade in the application of electron and ion imaging in TPEPICO experiments, and the implementation of such experiments at high intensity and high photon resolution synchrotron radiation facilities have resulted, and permitted the utilization of TPEPICO studies in an ever-widening range of applications. This review of the TPEPICO field will provide brief historical accounts of Threshold PhotoElectron Spectroscopy and TPEPICO, and then focus on the recent implementations of these advances at synchrotron radiation facilities.

2. Threshold Photoelectron Spectroscopy (TPES)

Threshold photoelectron spectroscopy had its origins in the Chicago area. An established photoionization mass spectrometry group, headed by Mark Inghram at the University of Chicago, added an electron extraction region to their experiment, followed by a 127^o electrostatic energy analyzer (see Figure 1). The electrons and ions were extracted perpendicular to the photon beam with an electric field of about 3 V/cm. The TPES was obtained by gently accelerating threshold electrons from the ionization region to 6 eV, and then passed them through the electrostatic energy analyzer at that energy. By scanning the photon monochromator, Villarejo et al.[5] obtained the TPES of rare gases with a resolution of about 40 and 50 meV as measured by the peak widths of the Xe ion TPES at the $^2P_{3/2}$ and $^2P_{1/2}$ states, respectively. These were in reasonable agreement with the expected resolution of 70 meV, based on the 6 volt electrons and slit sizes of the electron monochromator.[6] An additional complication, not discussed by Villarejo, is the energy spread of the threshold electrons that are born at various locations in a uniform electric field (see hashed area in the middle of the ionization region). In the University of Chicago experiment, the electrons were accelerated over a distance of about 2 cm to a final voltage of 6 eV. The spread of the photon beam emerging from the monochromator slits is about 0.2 cm at the midpoint of the ionization region. Thus in an applied electric field of 3 V/cm, the electrons will gain a final energy ranging from 5.7 to 6.3 eV, i.e. with an energy spread of 0.6 eV. This point will be discussed in greater detail later. Figure 2 shows Villarejo's spectrum for Xe which exhibits peaks with a width of about 50 meV.

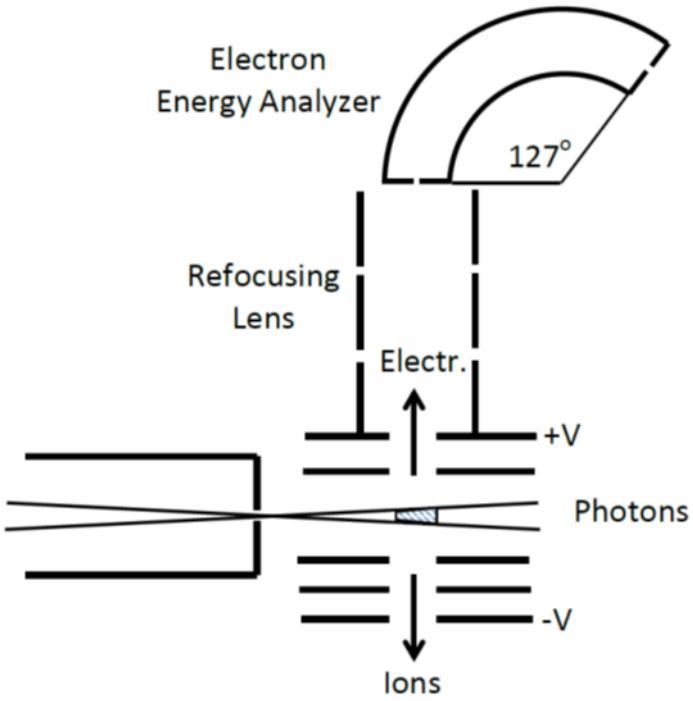

Figure 1. Diagram of first threshold

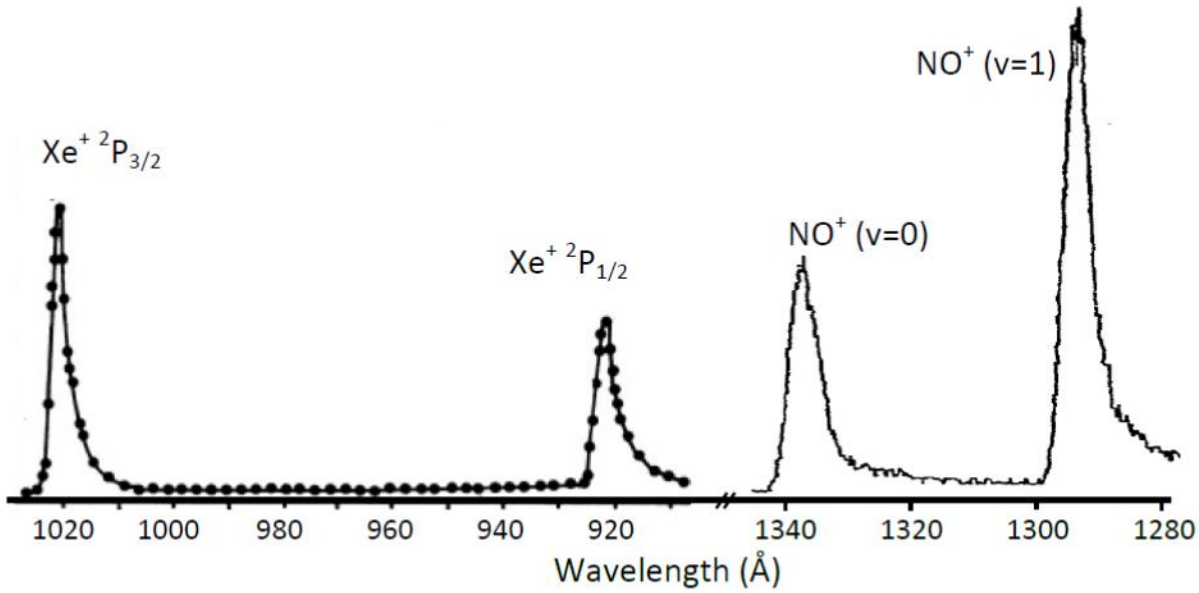

Figure 2. The first threshold electron spectra from the Inghram (Xe) and Schlag (NO) labs. Note the asymmetric peaks with the high energy tails caused by hot electrons. Adapted with permission from Villarejo et al.[5] and Baer et al.[7]

electron spectrometers.

A very similar approach was taken by the group of Ed Schlag, then at Northwestern University.[7,8] However, they incorporated a telescope after the photon monochromator in order to refocus the light at the center of the ionization region thereby reducing the thickness of the ionization region. But, because even this refocusing still resulted in an ionization region that was about 0.05 cm thick at the two ends, the accelerated electrons in the electric field of 3 V/cm had a dispersion of about 150 meV. For a variety of reasons, including low photon fluxes from the refocusing telescope and the large number of voltages on both the lens and energy analyzer that had to be adjusted, the signal level was extremely low. The only means for passing electrons through the 127° electrostatic analyzer was to remove the entrance and exit slits. In spite of this mode of operation which had a theoretical resolution of well over 1 eV, a scan of the TPES of nitric oxide (Figure 2) showed well resolved vibrational levels with peak widths that corresponded to a resolution of 35 meV. It was clear that the resolution did not emanate from the energy analyzer but from the fact that threshold electrons have a very high collection efficiency whereas energetic electrons, being ejected in all directions, have a collection efficiency that decreases rapidly with the electron energy. This was confirmed when the electron lens and energy analyzer were replaced by a simple 10 cm long tube with 6 mm apertures, and the resulting energy resolution remained at about 35 meV, but the signal level increased by a factor of 10.[7,8] This resolution was determined primarily by the convolution of the photon resolution and the natural line width of the rotational envelope of the NO TPES peaks.

The collection efficiency of electrons, C_{eff}, formed at an initial energy, V_0, in the center of the ionization region, accelerated to a final voltage, V, and then drift through a tube of length, d, is given by the expression:

$$C_{eff} = 1 - \left[1 - \frac{\Theta}{\pi}\left(\frac{V}{V_0} + 1\right)\right]^{\frac{1}{2}} \qquad when\ V_0 \geq V\frac{\Theta}{\pi} \qquad (2)$$

In this equation, Θ is the maximum solid angle into which the electrons are collected. It is defined by $\Theta = \pi(r/d)^2$ where *r* is the radius of the aperture in front of the electron detector, and *d* is the distance from the detector to the ionization region[9,10]. At sufficiently small initial electron energies ($V_0 \leq V(\Theta/\pi)$), all electrons will be collected and the collection efficiency, $C_{eff} = 1$. At higher electron energies for which equation (2) is valid, the collection efficiency drops rapidly. We can use the energy $V_0 = V(\Theta/\pi) = (r/d)^2V$ as a measure of the resolution. Similar expressions have been derived by Spohr et al.[11] and Baer et al.[7]

It is evident that the collection efficiency does not go to zero at high electron energy because there will always be some energetic electrons with an initial angle that can pass through the final aperture and be collected. Both spectra in Figure 2 show the asymmetry of the peaks and the tail extending toward higher energies. The history of TPES for the following 30 years was largely shaped by attempts to eliminate this "hot electron" tail. The hot electron contamination is directly proportional to the size of the final aperture. However, because the ionization region in laboratory vacuum UV light sources is rather large (ca 1 cm^2), reducing the size of the final aperture is not an option. In 1971 Spohr et al.[11] used collimated hole structures with thousands of holes on a stainless steel disc with a diameter of 1 cm to use the full ionization volume, yet maintain a small solid collection angle, Θ. The use of collimated holes to terminate the ionization region for both electrons and ions was used by the Baer group for a number of studies. A benefit of the collimated holes was the ability to operate with higher gas pressures, which were used to investigate ion-molecule reactions.[12] However, the major drawback of the collimated hole structures was electron collisions with the walls of the tubes which resulted in both reduced electron signal as well as channeling of hot electrons, so that the hot electron contamination

remained a problem. An approach similar to one shown in Figure 1, but in a manner that did not sacrifice signal levels, involved lengthening the electron drift tube to improve the electron energy resolution for threshold electrons and using the electrostatic analyzer simply to cut off the hot electron tail above an energy of 250 meV.[13] In order to minimize the voltage drop across the ionization region, it was necessary to operate with a low extraction field (ca 1.3 V/cm). Thus, adapting this approach to electron ion coincidence studies with good ion collection efficiency required Stockbauer[13] to pulse the ions out of the ionization region. Although this approach was successfully used for a number of studies,[14,15] a major disadvantage of ion pulsing is the difficulty in distinguishing false coincidences from true coincidences. This issue will be discussed later.

2.1 Detection of threshold electrons by time of flight

The fundamental problem in using an electrostatic energy analysis scheme to select threshold electrons is the voltage drop across the ionization region (see Figure 1) which imparts a broad range of final energies to the extracted electrons. On the other hand, a time of flight analysis avoids this problem when the electrons are extracted using Wiley McLaren space focusing conditions.[16] Tsai et al.[10] accomplished this using continuous laboratory VUV light source and pulsing the electrons out of the ionization region with a 3 MHz, 1 V pulse train. The acceleration (2 cm) and drift regions (4 cm) for the electrons were small so that the total time of flight for threshold electrons was about 80 ns. By gating the electron detector to accept signal only in a small time window centered at 80 ns, it was possible to completely avoid collecting hot electrons. The resolution of 25 meV was limited primarily by the photon bandwidth. A similar experiment was carried out at ACO, the synchrotron radiation facility in Orsay, France.[17,18] Because this light source was operated in the single bunch mode, the pulse structure of the light could be used as a start signal for collecting the electrons in a constant field of 1 V/cm, thereby greatly simplifying the experiment.

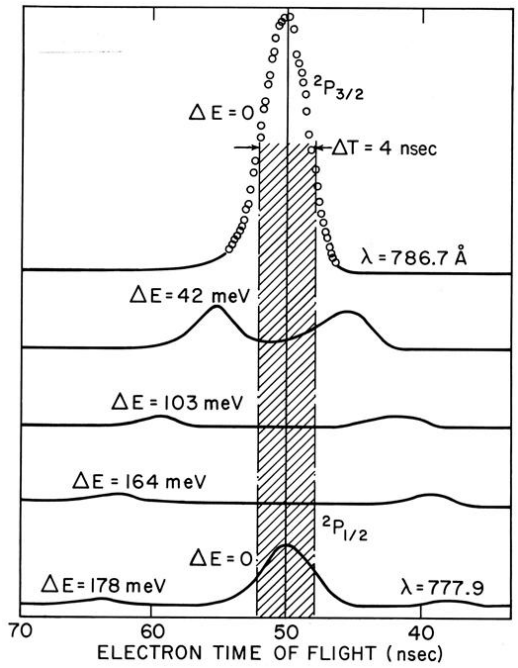

Figure 3. Electron TOF distributions for Ar at various photon energies from the IE to the second electronic state in a pulsed photoionization experiment at the LURE synchrotron in Orsay. Reproduced with permission from Baer et al.[17]

Figure 3 shows the TOF distribution for photoelectrons from argon at various photon energies obtained in the Orsay experiment. At the ionization limit (786.7 Å) only threshold electron are detected. At a photon energy of 42 meV above the Ar ionization energy, one observes the forward and backward scattered electrons at lower and longer TOF, respectively. The electrons ejected at right angles to the extraction axis, which would appear at 50 ns, have been lost. The hashed area shows that TOF window in which the true threshold electrons are detected. The electron resolution (about 10 meV) was limited mostly by the photon bandwidth of the 1 m normal incidence VUV monochromator. Although threshold electron spectroscopy by the TOF method worked extremely well, achieving good collection efficiency for ions in an electron ion coincidence experiment required the ions also to be pulsed out of the ionization region. As mentioned previously this mode of ion extraction results in a structured peak for any false ions that happen to be in the ionization region when the extraction pulse is applied. It necessitates collecting a randomly triggered ion time-of-

flight spectrum to generate a false coincidence spectrum that can be subtracted from the original one. In addition, dynamical information about ion dissociation rates or kinetic energy release distributions are more difficult to extract in a pulsed field. Nevertheless, a substantial body of work on both unimolecular and bi-molecular reactions with energy selected ions was produced by the Orsay group.[19-22]

One approach that uses an electrostatic energy analysis for threshold electron detection with no hot electron background is based on employing a vanishingly small electric field to extract the electrons. An early version of this was proposed by Peatman et al.[23] who replaced the "line of sight" analyzer by an analyzer that required the electrons to traverse an indirect path to the detector. Unfortunately, good resolution for threshold electrons and hot electron suppression only worked under conditions in which the collection efficiency for threshold electrons was very low. In addition, it was incompatible with the simultaneous extraction of ions, and thus not appropriate for electron-ion coincidence studies.

A much more effective and versatile approach based on electrostatics was developed by King and co-workers,[24] in which the ionization region was surrounded by a grounded cylindrical cage and threshold electrons were extracted by a weak penetrating field. Hot electrons drift to the walls, while electrons with energy less than 3 meV are gently extracted and focused at the exit hole of the cylinder, and then further analyzed by a 127° electrostatic energy analyzer. This results in the complete suppression of hot electrons, respectable collection efficiency, and a TPES resolution limited only by the photon bandwidth, which in some cases was 2 meV.[25-28] A subsequent version of this analyzer permitted ions to be extracted in the same manner making it compatible with threshold photoelectron photoion coincidence studies.[29] SIMION[30] calculations of the potential and electron and ion trajectories are shown in Figure 4. The interesting aspect of this spectrometer is its versatility which allows threshold electrons to be collected in coincidence with thermal ions whose mass is analyzed by TOF. However, mass resolution is not very good because the TOF is broadened in the early stages of ion extraction in the very weak field. In addition, fragment ions formed with kinetic energy have a collection efficiency that decreases with increasing kinetic energy.

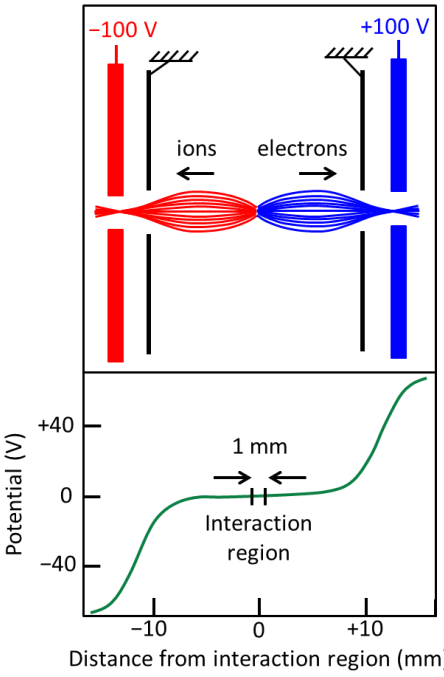

Figure 4 Electical field lines in the ionization region of the penetrating field approach to threshold electron detection. From George C. King (private communication).

The real power of the penetrating field approach, besides its ability to easily collect threshold photoelectron spectra with excellent resolution, was realized by reversing the voltage on the ion side so that both electrons in double ionization processes could be extracted in opposite directions and collected in coincidence (threshold photoelectron photoelectron coincidence, or TPEPECO).[31,32] That is, one detector is tuned to collect threshold electrons, while the other detector is tuned to collect electrons of slightly positive energy. Whilst initially applied to atoms, it was later appreciated that high-resolution spectra of vibrationally-resolved dications of molecules could then be determined with a resolution essentially limited to that of the photon source.[33]

2.2 Detection of threshold electrons by velocity map imaging

All methods for extracting threshold electrons described so far involved the use of low or very low electric fields in order to avoid collecting hot electrons. However, a fundamental problem involves the collection of threshold electrons from the dispersed ionization region, which has the height of the photon beam and a considerably larger width along the path of the photon beam. This problem was solved independently by two groups. As early as 1992, Hatherly et al.[34] introduced an achromatic electron extraction lens, which permitted threshold electrons from a large ionization region to be extracted by a substantial electric field of 20 V/cm and focused onto a small aperture, thereby discriminating against energetic electrons with off-axis velocity components, and simultaneously permitting ions to be extracted with high efficiency in a DC electric field. Just as in the original design of Villarejo et al.[5], the on-axis hot electron tail was reduced by the use of a 127° post analyser. However, the limited photon resolution of 20 meV from the 1 m Seya-Namioka photon monochromator used for the majority of their experiments at the Daresbury synchrotron did not permit a determination of the experimental electron resolution, which SIMION[30] modeling suggested should be on the order of a few milli-electron volts only.[34] Experiments at improved resolution using the 5 m McPherson monochromator at Daresbury confirmed that the resolution of the experiment was indeed limited by that of the monochromator, not that of the electron analyser.[35]

A more versatile approach first used in laser multi-photon ionization studies was developed by Eppink and Parker in 1997[36] in which charged particles of all energies could be dispersed by a simple aperture lens and focused according to their velocity in the direction perpendicular to the extraction axis. The extracted particles were dispersed and collected on imaging plates on which the various initial kinetic energies of the charge particles were displayed in the form of rings whose radii are proportional to the initial velocities perpendicular to the extraction axis. This approach was later adopted by Baer and Li[37] for the collection of threshold electrons in their TPEPICO experiment. Much as in the Hatherly[34] apparatus, the real power of this approach for threshold electrons is that they can be focused down from a large ionization region to a sub-millimeter spot in the center of an imaging detector. When this was first tried, the flux of electrons increased by a factor of ten and the resolution improved by a factor of more than two, and was limited mostly by the photon monochomator.[37] Although hot electrons are not eliminated completely, they are greatly suppressed mainly because the old 5 mm aperture was replaced by a 1 mm aperture, thus reducing the open area by a factor of 25.

It is interesting to compare these velocity focusing methods with the weak penetrating field approach of King et al.[24] Both methods focus threshold electrons but they do so with very different electric fields. In velocity focusing, the field in the ionization region can be quite large, up to 100 V/cm, whereas in the weak penetrating field approach, the field is vanishingly small. In the penetrating field approach, the voltage drop across the width of the photoionization region is so small that the initially zero energy electrons can be effectively energy analyzed by a dispersive analyzer, so that hot electrons can be totally suppressed by the analyzer. On the other hand, in velocity focusing methods, initial hot electrons, whose velocity is directed parallel to the electric field will be collected in the central focusing spot, and

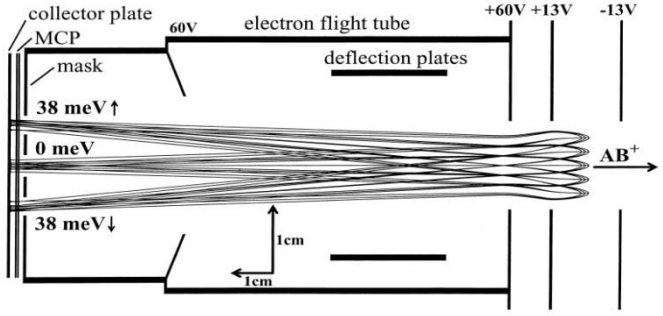

Figure 5 SIMION[30] calculations of 0 and 38 meV electrons ejected isotropically from a dispersed ionization region. The purpose of the deflection plates was to steer the threshold electrons onto the 1 mm aperture in the center of the MCP detector. Reproduced with permission from Sztáray and Baer[38]

there is no method for distinguishing them from the true zero energy electrons. That is, hot electrons are suppressed but not eliminated by velocity focusing, explaining the need for the 127° post analyser in the apparatus of Hatherly et al.[34]

The final challenge in the velocity focusing experiment is thus to account for the hot electrons. This was accomplished by Sztaray and Baer[38] utilizing a multichannel plate detector with two anodes; one collects electron signal hitting the center, and the other collects electrons hitting a ring around the center. The purpose of the ring detector was to collect only hot electrons, while the center detector collected both the threshold electrons and the background of hot electrons. Figure 5 shows a diagram of the ionization and electron extraction optics, with SIMION[30] modeling of the electron trajectories starting at various locations in the ionization region for two different electron energies. Subtracting the former from the latter results in a pure threshold electron spectrum. This subtraction procedure is best achieved when the electrons are detected with an imaging detector because the choice of the center spot and the location and size of the ring around this spot can be optimized for best resolution and hot electron subtraction. The reason this subtraction scheme has a chance of working is that all hot electrons contribute a small fraction of signal at the center spot (Figure 6). The result is a build-up of unstructured hot electron signal over the whole plate, including near its center where the true threshold electron signal resides. Those hot electrons which contaminate the true threshold electron signal can thus be subtracted by sampling the hot electron signal next to the center.

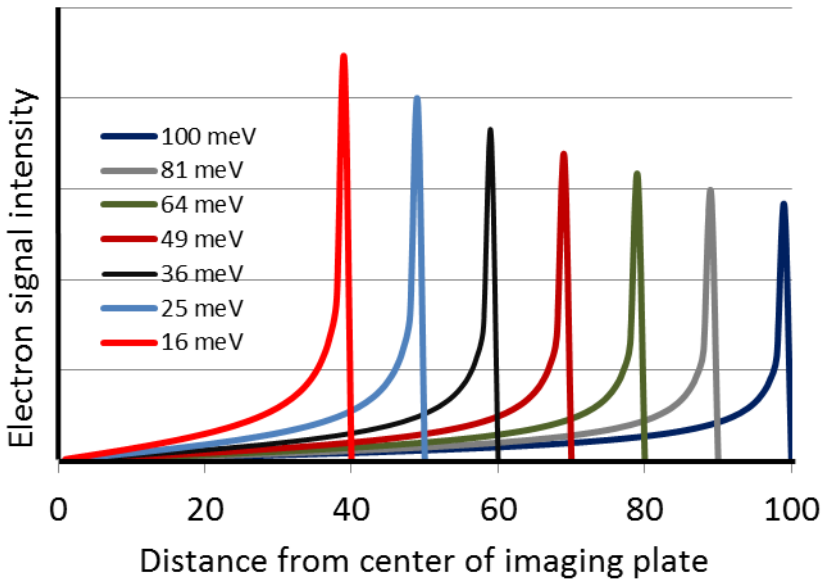

Figure 6. Calculated radial distributions of electron intensities for 7 electron energies on an imaging plate.

An example of the subtraction is shown in Figure 7 (from one of the authors' laboratory in Chapel Hill) in which the photoelectron signals for acetylene collected in the central and ring electrodes are plotted as

a function of the photon energy, along with the subtracted signal. At the ionization energy of about 11.4 eV, the electron signal consists exclusively of zero energy electrons which all hit the central electrode (blue signal) with no spill over on to the ring electrode. By 11.45 eV, the only electrons are ones having about 50 meV of energy, some of which get focused onto the ring electrode. However, these 50 meV (hot) electrons are ejected more or less isotropically so that the electron energies directed perpendicular to the extraction axis vary from zero to 50 meV. The ones with a low energy perpendicular to the extraction axis get focused onto the central electrode, which accounts for the blue signal at 11.45 eV. Such a highly structured TPES near the ionization threshold is, in fact, not an ideal situation for illustrating the subtraction procedure because the structured ring signal can introduce unwanted structure in the subtraction process and even result in negative signals. However, even in this case, the procedure works reasonably well. As the molecules get larger and the TPES more complex,

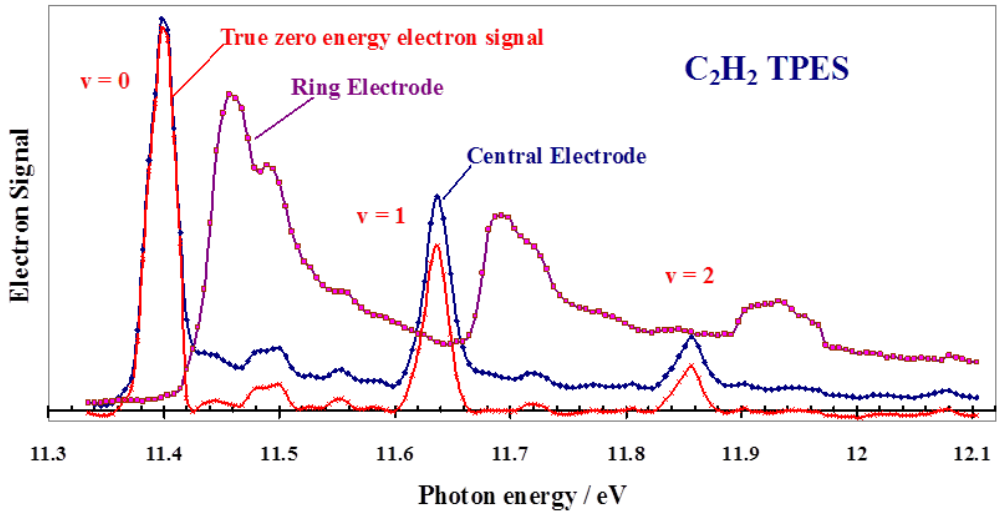

Figure 7. A TPES of acetylene showing the ionization energy and the excitation of the first two symmetric stretch vibrations. The blue and purple lines are the central and ring electrode signals, while the red line is the subtracted signal. Before subtraction, the ring signal is normalized by the ratio of surface area of the two detectors.

especially at higher energies, such issues become less of a problem. The resolution in Figure 7 is limited by the 1 m photon monochromator. The much higher photon resolution available at the VUV beamline of the Soleil (France) synchrotron permitted Garcia et al.[39] to obtain a resolution of 0.8 meV on the Ar ion TPES peak.

2.3 TPES, pulsed field ionization (ZEKE) spectroscopy, and the Stark Effect

The development of tunable lasers, especially pulsed lasers, in the 1980s provided convenient light sources for the study of ions by resonant and non-resonant multi-photon processes.[40] The much higher resolution of these lasers compared to vacuum UV spectrometers provided an opportunity to improve greatly the resolution of threshold photoelectron spectroscopy.[41] In that study, Mueller-Dethlefs et al. noted that the measured NO ionization energy "is 4.3 cm^{-1} lower than the value obtained previously by Miescher from the extrapolation of the Rydberg f-series." In addition, Mueller-Dethlefs *et al.*[42,43] found that a pulsed electric field was far superior to a DC extraction scheme, and that the longer the delay

between the photon pulse and the extraction pulse, the better the resolution. In fact, the best scheme utilized a very small field to remove directly produced electrons and ions from the ionization region, followed by a pulsed field of 1-2 V/cm. It soon became evident that the mechanism for this process was pulsed field ionization (PFI) of long lived (up to several μs), high *n* Rydberg states.[44] Because Rydberg states directly accessed from the neutral precursors have modest ℓ quantum numbers with lifetimes much less than a microsecond, the production of long-lived states could only be explained by ℓ mixing made possible by external electric and magnetic field perturbations, provided perhaps by the high density of ions created in the focus of the high intensity pulsed laser field.[45-47]

PFI-ZEKE and TPE spectroscopies differ in two ways. PFI-ZEKE is best carried out with pulsed lasers which provide a small plasma of ions and electrons yielding the inhomogeneous fields required for ℓ mixing, whereas the TPE spectrum can be collected with either continuous or pulsed light sources. Secondly, the high *n* Rydberg states ionized by PFI necessarily lie below the ion energy, so that the observed peak energies are below the true ion energies. How much less is a function of the small DC field as well as the magnitude of the pulsed field. The Stark shift, or energy depression in an electric field is given by:[48]

$$\Delta E = \frac{1}{2}\sqrt{\frac{eF}{\pi\varepsilon_o}} \cong 6\sqrt{F}\ cm^{-1} \qquad (3)$$

where *F* is the electric field. With units of V/cm for the electric field, the second part of the equation gives the Stark shift in units of cm^{-1}. Thus a typical Start shift for a 1 V/cm electric field pulse is 6 cm^{-1} or about 0.8 meV.

In the case of TPES with a continuous light source (which does not generate a micro-plasma of electrons and ions, and thus does not stabilize long lived Rydberg states), the bulk of the signal comes from low energy electrons, which have an asymmetric tail toward higher energies (see Figure 2). Thus, if the photon monochromator resolution is sufficiently narrow, the TPES peak widths will be determined by the electron resolution. The convolution of a symmetric (e.g. Gaussian) photon profile with a quasi-exponential TPES resolution profile leads to a net TPES peak that is shifted slightly to higher energy. On the other hand, if the experimental resolution is limited by the photon source, then the peaks will be symmetric and the true ion state will be located at the maximum of the TPES peak.

An interesting and as yet not fully understood issue concerns the Stark effect in the TPES. Earlier TPES and TPEPICO experiments that used low extraction fields and had modest energy resolution clearly were not affected by such shifts. However, experiments at the Swiss Light Source (SLS) synchrotron routinely use extraction fields on the order of 120 V/cm, which according to eq. (3) should result in a shift of 66 cm^{-1} (ca 8 meV). Such a large shift should easily be observable with the threshold electron resolution of 2 meV, as indeed was found by Savee et al.[49] for the case of the benzyl radical IE. Similar Stark effects have been observed by Bodi et al.[50] for the Ar, N_2 and CH_3I Ã state TPES with shifts that are in near perfect agreement with Eq. 3. However, a careful study of the IE on fluorinated ethenes with extraction fields between 20 and 120 V/cm found no evidence of a shift.[51] To further confuse the issue, it has been reported that the ionization energy to ground state of methyl iodide is not subject to a Stark shift, while the A state is shifted.[50] Finally, no evidence was observed of a Stark shift in the measured dissociative photoionization onsets in CH_4 and CH_3I.[50] These seemingly contradictory results suggest that the Stark shift may be important when the photoexcitation involves the excitation of long lived Rydberg states (as is always the case in pulsed field ionization) but not when the process is dominated by direct ionization.

The only means for distinguishing which type of ionization process is operative therefore involves measuring the onsets at two or more extraction fields, and extrapolating the onset to zero field.

The long delay times associated with PFI-ZEKE (also called ZEKE) spectroscopy permitted directly produced ions and electrons to drift out of the ionization region in the small applied electric field. The remaining high-*n* Rydberg states could then be field ionized into electrons and their ions. Johnson and Zhu[52] took advantage of this fact by detecting the ions produced from the long-lived Rydberg states, calling the technique Mass Analyzed Threshold Ionization (MATI). This technique can be very useful when the sample contains a mixture of molecules, as might be the case in a combustion experiment or a molecular beam source with a distribution of dimers, trimers, *etc*. In addition, it can be used to determine the dissociation limits of ions.[53,54] From an experimental point of view, MATI is more challenging because a larger electric field prior to the ionization pulse is required in order to move the directly produced ions out of the ionization region.

Although continuous light sources, such as a synchrotron do not have sufficient intensity to stabilize efficiently long-lived high-*n* Rydberg states, pulsed field ionization does still work, but with a low yield of electrons.[55] A large body of work, mostly on small molecules, has been reported by the group of Ng.[56-61]

3. Photoelectron Photoion Coincidence Mass Spectrometry

The combination of ion detection in delayed coincidence with energy selected electrons was accomplished soon after the development of PES[62-64] and TPES.[12,65] The threshold photoelectron photoion coincidence (TPEPICO) approach has several major advantages over the fixed photon energy PEPICO experiment. Firstly, threshold electrons can be collected with high collection efficiencies (25-75%) whereas the energetic electrons used in PEPICO are collected with less than 1% efficiency. Secondly, the fixed photon energy PEPICO approach generates a constant high flux of electrons and ions, no matter what range of energies are of interest. On the other hand, in the TPEPICO experiment the photon energy is tuned to equal the ion energy of interest so that the number of electron and ions generated is always at the lowest possible level. This means that the false coincidence events for a given signal rate are always less in TPEPICO than they are in PEPICO studies. Thirdly, in TPEPICO (unlike in PEPICO) it is possible to optimize simultaneously the threshold electron resolution, the ion collection efficiency, and the ion mass resolution. Finally, it can be of interest to study autoionisation and non-Franck-Condon effects, and the strict applicability or not of the vibronic selection rules when operating under threshold electron conditions.[66-69]

3.1 Coincidence Statistics

In the absence of photon induced electron emission from a surface, every ionization event produces one electron and one ion, the latter being either the parent ion or the daughter ion. In TPEPICO only threshold electrons are detected, which depending on the electron resolution, photon energy and photoelectron yield, can vary in collection efficiency between 0.01 and 100%. At the ionization threshold, all electrons have zero energy so that their collection efficiency is a maximum, limited only by the detection optics and the detector efficiency. For a total ionization rate of N s^{-1}, the electron and ion signals are given by:

$$N_e = \eta_e N \quad \text{and} \quad N_i = \eta_i N \qquad (4)$$

where η_e and η_i are the collection efficiencies of electrons and ions, respectively.

The number of ions collected in coincidence with a zero energy electron is equal to the electron start rate times the ion efficiency, or $N_c = \eta_i N_e$. Equivalently, it can be expressed in terms of the ion rate and the electron collection efficiency as $N_c = \eta_e N_i$. These two equations permit the determination of the electron and ion collection efficiencies from the observed count rates as:

$$\eta_e = N_c/N_i \text{ and } \eta_i = N_c/N_e \qquad (5)$$

Determining the electron and ion detection efficiencies is an extremely valuable diagnostic tool for optimizing the instrumental performance, and a combination of equations (4) and (5) leads directly to the total ionization rate, N. An important assumption implicit in these equations is that the collected electrons and ions originate from the identical volume in the ionization region. For instance, if the ions are collected from a larger region, the measured electron collection efficiency will be too low, and vice versa. The collection efficiency also depends upon the electron and photon energy resolutions. If the photon resolution is much broader than the electron resolution, then at the ionization threshold, many of the electrons will be energetic and will not be detected, thereby yielding an artificially low electron collection efficiency. At higher photon energies only a fraction of the electrons are threshold electrons so that it is no longer possible to determine the instrumental electron collection efficiency (unless the higher energy electrons are detected on an imaging plate). But, the parent ion efficiency should remain constant. On the other hand, the fragment ion collection efficiency may decrease if the translational energy release upon dissociation becomes sufficiently large to prevent them from hitting the detector.

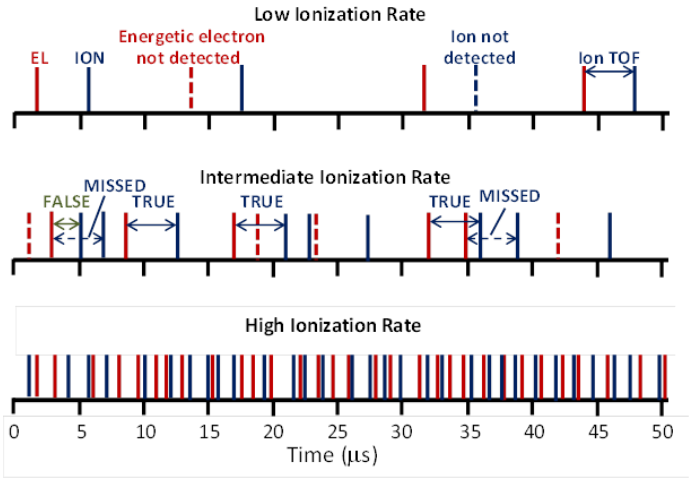

Figure 8 Electron and ion signals collected under three different ionization rates. At low rates, nearly all coincidences detected are "true". At intermediate ionization rates some "false" events are detected because of ionization events that overlap in time, and some true coincidences are missed. In the limit of high ionization rates, the overlap of ionization events is massive.

The collection efficiency for both electrons and ions can also be reduced by coincidence statistics, primarily due to the false coincidences. As shown in Figure 8, in the limit of low ionization rates the collection of an electron and its ion is well separated in time from the subsequent event. The solid lines indicate electrons and ions actually collected, the dashed lines indicate those not detected, which could be a result of detectors that are not 100% efficient, and in the case of electrons because they are energetic. In the snapshot illustrated, two out of four of the ionization events are collected as true coincidence events. For intermediate ionization rates, ionization events overlap so that the first ion detected may not be associated with the preceding threshold electron. Such false coincidences appear at random times and are thus not time correlated to the detected threshold electron signal. Finally, at high ionization rates, the individual ionization events overlap massively so that the true coincidences are not readily apparent.

The early coincidence experiments used time to pulse height converters (TPHC) to record the coincidence event and the ion flight time. A logic pulse from the electron detector was used as an input, and a similar ion pulse was used as the stop pulse. The output, which consisted of a voltage pulse (between 0 and 10 V) whose amplitude was proportional to the time difference, was then recorded on a multichannel pulse height analyzer. Once a start pulse initiated the timing event, no further start pulses were accepted. Similarly, the ion stop signal stopped the TPHC so that no further ion signals would be accepted. This set up, which is an example of a single start - single stop (SS) scheme, has the advantage of very precise ns timing. But, its use is limited to low flux experiments because of the large dead time and a significant number of ionization events are missed. For instance, in the intermediate ionization rate case shown in Figure 8 a true coincidence event is missed because the preceding false ion stopped the TPHC. Similarly, a second true coincidence event is missed because the threshold electron signal is missed because a preceding electron started the timing sequence so that no further start signals are accepted until the TPHC resets itself. As the ionization rate increases, the false ions invariably stop the timing sequence before the true ion is detected. It is possible to collect more of the ions by the use of a multistop approach (SM) in which the TPHC is replaced by a multichannel scalar that can accept multiple stops. Such instruments sacrifice timing precision, and they do not solve the problem of missed start signals. As discussed by Bodi et al.[70] the only sensible approach for collecting coincidence data at high acquisition rates is to use a multi-start multi-stop (MM) configuration in which all electron and ion signals are collected and timed relative to a master clock. In this manner, all electron and ion signals are collected and the un-correlated false coincidences appear as a flat background.

The true coincidence rate, c_T, for the case of the MM set up can be expressed as the product of the detector collection efficiencies, η_e , η_i , and the total ionization rate N, so that $c_T = N\eta_e\eta_i\ s^{-1}$. The true coincidences are time correlated so that these counts appear in the form of a peaks in the TOF spectrum which correspond to the flight time of either the parent or the various fragment ions. On the other hand, the false coincidence rate in a given time window, w, is not time correlated and is proportional to the square of the total ionization rate, and is thus given as $c_F = N^2\ \eta_e\eta_i\ w\ s^{-1}$. These relations lead to the following useful equations:

$c_T = N\eta_e\eta_i$ True coincidence rate (s^{-1}) (6)

$c_F = N^2\ \eta_e\eta_i\ w$ False coincidence rate (s^{-1}) (7)

$C_T = r\ N\ \eta_e\eta_i\ \tau$ Total true coincidence counts for a given mass peak with a fractional intensity of r, and a collection time, τ. (8)

$C_F = N^2\ \eta_e\eta_i\ w\ \tau$ Total false coincidence counts in a given time window and a collection time, τ. (9)

$\frac{S}{N} = \frac{C_T}{\sqrt{C_F}} = r\sqrt{\frac{\eta_e\eta_i\tau}{w}}$ Signal to noise ratio contributed by the false coincidence background for a given coincidence peak with w = peak width. (10)

$\frac{S}{N} = \frac{C_T}{\sqrt{C_T}} = \sqrt{C_T} = \sqrt{rN\eta_e\eta_i\tau}$ Signal to noise ratio contributed by the counting statistics of the true coincidence peak. (11)

The signal to noise ratio of the true coincidence peak arises from two sources, which are the counting statistics of the flat false coincidence background as well as the counting statistics of the coincidence peak itself. These contributions are shown by equations (10) and (11). Two points can be made. Firstly, it is evident that even though the false coincidence count rate increases with the square of the total ionization rate, *N*, its contribution to the noise of the coincidence peak is independent of *N.* Because the signal-to-noise ratio in the true coincidence peak increases also as the square root of the total count rate, it is clearly best to operate at high photon fluxes. Secondly, as expected, high collection efficiencies, narrow peak widths, and long collection times all contribute to good signal to noise.

3.2 Optimizing both electron energy and ion mass resolution

Good ion mass resolution in a linear time of flight (TOF) mass spectrometer is usually accomplished by two acceleration regions followed by a single drift region. Voltages are adjusted to conform to the Wiley McLaren space focusing conditions,[16] in which equal mass ions produced at various positions in the ionization region end up with the same TOF just as they reach the ion detector. The key to good electron energy resolution by velocity focusing optics is the use of a very gentle lensing action that extracts the electrons out of the ionization region followed by a long electron drift tube. This is best accomplished by an acceleration region that has a nearly constant electric field. The rather strong second acceleration for the ions should be placed as far from the ionization region as is practical to avoid penetrating fields through the grids that separate the low field first region from the high field second region. This is not usually done because essentially all commercial two-stage linear TOF instruments have two short acceleration regions. There is a second reason for using an extended (e.g. 5-10 cm long) first acceleration region in TPEPICO experiments which is that the ion TOF distribution contains important dynamical information about the rate of ion dissociation. An extended first region is particularly useful for measuring slow rates, which are (as explained later) essential for determining dissociative photoionization onsets.

3.3 Optimization of ion mass resolution

The mass resolution of a TOF spectrometer depends on several factors, including the temperature of the sample, the magnitude of the electric field in the ionization region, and the total time of flight of the ions. It also depends on whether the mass peak of interest is a parent or a fragment ion, because the latter is broadened by translational energy release during the dissociation process.

In a perfectly designed TOF MS instrument, either of a linear or reflectron (ReTOF) design, the parent ion peak width is determined only by the translational temperature of the sample, the ion mass, and the electric field in the ionization region. For a thermal sample with a Maxwell Boltzmann distribution at a temperature, T, the peak should have a Gaussian shape whose full width at half maximum (*fwhm*) is given by: [2,13,71,72]

$$fwhm = \frac{\sqrt{8\ln(2)MRT}}{qF} \; or \; 0.02233\frac{\sqrt{MT}}{F} \qquad (12)$$

In this equation, *M* is the ion mass, *R* the gas constant, *T* the temperature, *q* the electronic charge and *F* the electric field. In the parameterized (second) part of the equation, the constants have been evaluated so that *M* is in units of amu, *T* in K, *F* in V/cm, yielding the full width half maximum of the peak in microseconds. This equation can be useful to determine either the temperature of the sample or, if the temperature is known, determining if the TOF configuration is optimized for best resolution. It is important to recognize that the peak width is sensitive only to the translational temperature, which in the case of a molecular beam is generally lower than the internal vibrational or rotational temperatures. Secondly, in the case of a molecular beam or a needle inlet, the translational temperature is not isotropic and refers only to the temperature in the direction of the ion extraction.

The peak width due to the thermal temperature of the sample is the same in a linear TOF as in a ReTOF. The improved mass resolution realized in the ReTOF configuration is a result of the increased flight time achieved by slowing the ions down and then accelerating them again in the reflectron. In fact, a similar gain in resolution could be achieved in a two-stage linear TOF but the final acceleration voltage and the drift distance would have to be increased beyond a practical level. The ReTOF instrument has some advantages for analyzing H loss product ions, as well as for the study of ion dissociation dynamics, especially in multiphoton experiments.[73,74] However, for slowly dissociating (metastable) ions in which neutral fragments have a substantial mass, the product ions are difficult to reflect with good collection efficiencies. This is especially true of ions that dissociate in the reflectron itself. Because ions can spend as much as 50% of their time in the reflectron, this loss of ion signal can be deleterious. As will be pointed out in the study of metastable ions, dissociation rates can also be investigated in a linear TOF apparatus with a two-stage drift region.

3.4 Measurement of translational energy released in ion dissociation steps

When the ion has sufficient energy to dissociate, it does so with the release of some translational energy and the peak becomes broader. Thus, in any given TOF mass spectrum, the fragment ion TOF peaks are broader than the parent ion peaks, after the difference in their masses are taken into account. With the assumption that the translational energy released in the dissociation is statistical and isotropic, the average translational energy released (<KER>) in the dissociation can be extracted from the fragment ion Gaussian-shaped peak widths using the following equations: [13,72]

$$< KER > = \frac{M}{(M-m)m}\frac{3}{15\ln(2)}(qF)^2(fwhm)^2 - \frac{m}{(M-m)} < E >_{th}$$

$$or < KER > = 0.2606\frac{M}{(M-m)m}(F)^2(fwhm)^2 - \frac{m}{(M-m)} < E >_{th} \qquad (13)$$

In the second equation, the units of *M* (parent mass) and *m* (daughter ion mass) are in amu, *F* in V cm^{-1}, *fwhm* in μs, and <KER> and $<E>_{th}$ in units of eV. The term *M*/(*M*-*m*) takes into account the partitioning of the total translational energy between the neutral and ionic products. For instance, if the dissociation involves H loss from CH_4^+, then most of the translational energy is given to the H atom in order to conserve momentum; the mass ratio term is then 16. The fragment ion peak width has two contributions: one from the energy released in the dissociation process, and the other from the initial

translational energy from the parent ion. In order to obtain the energy released in the dissociation, the second term in equation (13) subtracts the contribution from the parent ion thermal energy.

If a goal of an experiment is the determination of the translational energy that is released in the dissociation, it is best to operate with a low extraction field because for a given KER, the fwhm of the fragment ion is inversely proportional to the extraction field. If the dissociation involves a simple bond rupture with no reverse activation barrier, then the ion energy in excess of the dissociation limit will be statistically partitioned among the translational and internal vibrational and rotational degrees of freedom, so that the fragment ion peaks will have Gaussian shapes.[75] In fact, Klots[76] showed that it is possible to assign a "temperature", T^*, to the dissociating system with the following equation:

$$E_{EXC} = E_V(T^*) + E_R(T^*) + E_T(T^*) \qquad (14)$$

where E_{EXC} is the excess energy above the dissociation limit, and the three terms on the right are the average vibrational, rotational, and translational energies in the center of mass. That is, the initial translational temperature of the parent ion is not included in $E_T(T^*)$. T^* is a fictitious temperature which is only approximately appropriate, but becomes progressively more meaningful as the size of the molecule increases. The average vibrational energy can readily be expressed as a sum over vibrational modes in terms of their vibrational partition functions. The rotational and translational energies can be expressed classically as $dRT/2$, where d is the number of rotational or translational degrees of freedom.

If the dissociation involves a barrier along the reaction coordinate, then it is possible that a significant amount of the energy associated with the reverse barrier is converted to translational energy of the products. In this case, the fragment ion peak shape may exhibit a flat top or even have two peaks, which correspond to fragment ion ejection in the direction of, or opposite to, the extraction field.[77] When the products are ejected with sufficient energy perpendicular to the extraction axis, their trajectories cause them to miss the detector.

A non-statistical translational energy release distribution may also arise from a dissociation that originates on a repulsive potential energy curve. In some cases, this involves dissociation from an excited electronic state that is repulsive,[78] and in other cases it may happen from the ground state of the cation. The latter include CF_4^+, CCl_4^+, and SF_6^+, all of which are unstable and dissociate even at the lowest photon energies via loss of a halogen atom.[35,79-81]

Fluorescence from excited states of polyatomic ions which lie at energies several eV above thermodynamic dissociation thresholds may also be regarded as another manifestation of non-statistical, 'isolated-state' behaviour.[81] Although not of direct relevance to this paper, we mention that in such instances coincidences can then be recorded between either photoions and fluorescence photons (PIFCO spectroscopy) or threshold photoelectrons and fluorescence photons (TPEFCO spectroscopy).[82-85] An apparatus, where any two of threshold electrons, ions characterized by their time of flight, and undispersed fluorescence photons can be detected in coincidence, is described with relatively trivial interchange between the three coincidence experiments.[81] PIFCO spectroscopy can determine the lifetime, τ, and fluorescence quantum yield, Φ_F, of the fluorescing state of the ion, but they are averaged over the Franck-Condon populations of vibrational levels of the fluorescing state. By observing which ion is detected in coincidence with the photon, the fate of the lower electronic state to which fluorescence occurs can be determined; an example is the $SiCl_4^+$ $C\ ^2T_2$ state fluorescing to both the repulsive $A\ ^2T_2$ state, in which photons are detected in coincidence with fragment $SiCl_3^+$, and the bound $X\ ^2T_1$ state, in which photons are detected only in coincidence with the parent ion.[35,81] TPEFCO

spectroscopy also determines τ and Φ_F and, with sufficient resolution in the photon source and electron analyzer, vibrational state selectivity of the fluorescing state is often achieved. Changes of τ and Φ_F with vibrational level are the most interesting because they can be attributed to a change, possibly onset, of a competing dissociative channel; a good example is the $C\ ^2T_2$ state of CF_4^+.[35,81]

3.5 Measurement of ion dissociation rates

The importance of ion dissociation rate measurements can hardly be overstated. First of all, most moderate to large ions dissociate slowly in the vicinity of their dissociation thresholds. Furthermore, many dissociation rates at threshold are sufficiently low that the ions dissociate during the course of acceleration or even while passing through drift regions. It is often the case that fragment ions appear only at energies far above their true thermodynamic energy thresholds with an apparent onset that exceeds the thermochemical onset, thus giving rise to the so-called "kinetic shift".[86-88] If the goal of the experiment is the measurement of such thresholds, then it is essential that the experiment be designed not only to recognize signs of a slow dissociations, but also to measure the dissociation rate as a function of ion internal energy in order to extrapolate the rates down to the onset, and thus account for the kinetic shift. Slow dissociations are also frequently observed in small ions, in which the metastability arises from tunneling through barriers. These are quite common in dissociations involving rate limiting H or D atom transfer or simply C-H or C-D fragmentation steps.[89-98]

The experimental feature that enables the measurement of ionic dissociation rates in TPEPICO experiments is an extended (5-10 cm) first acceleration region, which has a very uniform electric field. This permits measurement of dissociation rates between $5 \times 10^4 - 10^7\ s^{-1}$. In order to measure rates down to *ca.* $10^3\ s^{-1}$, it is also necessary to add a final deceleration region to the drift region so that ions that dissociate in the first part of the drift region can be measured as well. A diagram of such an instrument is shown in the upper part of Figure 9.[99] The decay of an energy selected ion (bromobenzene is shown as an example) fragmenting by single exponential decay is depicted in the lower left. The blue region is the time during which the parent ion accelerates in the first acceleration region. The resulting fragment ions have a TOF shown by the asymmetric blue peak in the lower right. These ions spend very little time in the short acceleration region; those that do have fragment time of flights somewhere between the blue and the red parent ion peaks. Some fragment ions are born while the parent ions traverse the first (green) drift region between 8 and 23 μs. If the drift region were composed of a single region, the latter fragment ions would have approximately the same TOF as the undissociated parent ions because they have the same velocity. However, their kinetic energy is reduced by the ratio of the fragment to parent mass ratio. Therefore, the deceleration field between the green and red regions slows those fragment ions down more than the parent ions, so that the former have a longer TOF and appear as the green peak in the TOF spectrum. This green peak can be shifted to different TOF depending on the applied deceleration field. The parent ions that never dissociate appear as normal parent ions and are represented by the red peak, here shown as a doublet because of the two Br isotopes.

It is evident from Figure 9, taken from Stevens et al.[99], that from the blue region of the TOF spectrum, we obtain differential rate information over the first 8 μs, and determine whether the rates are characterized by single exponential decay or bi-exponential as found for the case of pentene ion

dissociations.[100] The rate measurements can be extended to longer decay times by taking into account the integrated signal intensity from 8 to 24 µs from the area of the green peak. That is, by varying the photon energy and thus the ion internal energy, we can obtain dissociation rate constants ranging, in favorable circumstances, from 10^2 to 10^7 s^{-1}.[99] The loss of Br from the bromobenzene ion is a favorable case because the mass difference between fragment and parent ion is large, thereby yielding a broad asymmetric TOF peak (blue peak in Figure 9). The accessible rate constant range for H-atom loss from polyatomic ions is considerably less.

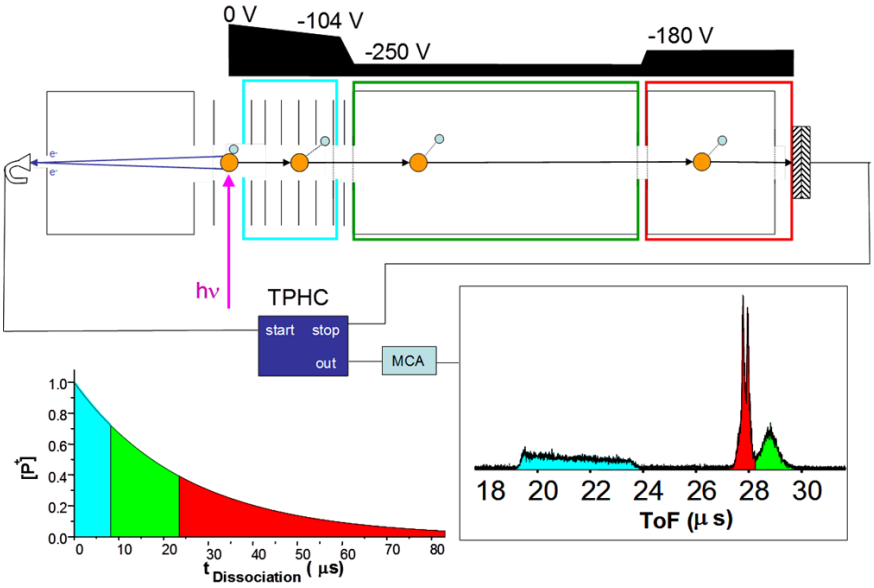

Figure 9. Experimental arrangement of an iPEPICO experiment designed to measure the ion dissociation rate constant. The blue section is the first ion acceleration region, which is followed by a short acceleration region to bring the ions to 250 V. The ions then drift at this energy through the green drift region. They are then decelerated and enter the final red drift region. Ions that dissociate in the blue region (0-8 µs as shown in the real time decay lower left) appear as the dispersed blue peak in the TOF spectrum. Fragment ions that decayed in the green region appear as the green peak in the TOF spectrum. Finally, undissociated ions of those that decay in the red region appear as the red peak. The figure is adapted with permission from Stevens et al.[99]

In the case of slow dissociations involving H loss, the fragment ion peak does not have a well-defined exponential shape. However, the peak is shifted toward longer TOF so that its center of gravity can be modeled to extract the rate constants.[101] An example is shown in Figure 10 for the case of H loss from ethanol.[98] The asymmetry is hardly noticeable, but the shift in the peak position for the CH_3CHOH^+ fragment ion is definitely visible. The center of gravity of this peak can be calculated from the following equation:

$$CoG = \frac{\int_{\tau_{min}}^{\tau_{max}} \tau I(\tau)}{\int_{\tau_{min}}^{\tau_{max}} I(\tau)} \qquad (15)$$

in which τ is the TOF, $I(\tau)$ is the TOF peak intensity, and integration is over the peak width. When these center of gravities are plotted *vs.* ion internal energy, we obtain the fitted breakdown diagram shown in Figure 11. The green data and the green abscissa on the right show the evolution of the CoG in μs as a function of the ion internal energy. At low energies that correspond to slow dissociation events, the peak center is shifted to longer TOF. At high energies (> 10.88 eV) the center of gravity reaches a constant value which corresponds to the TOF of rapidly dissociating ethanol ions. These rate data help

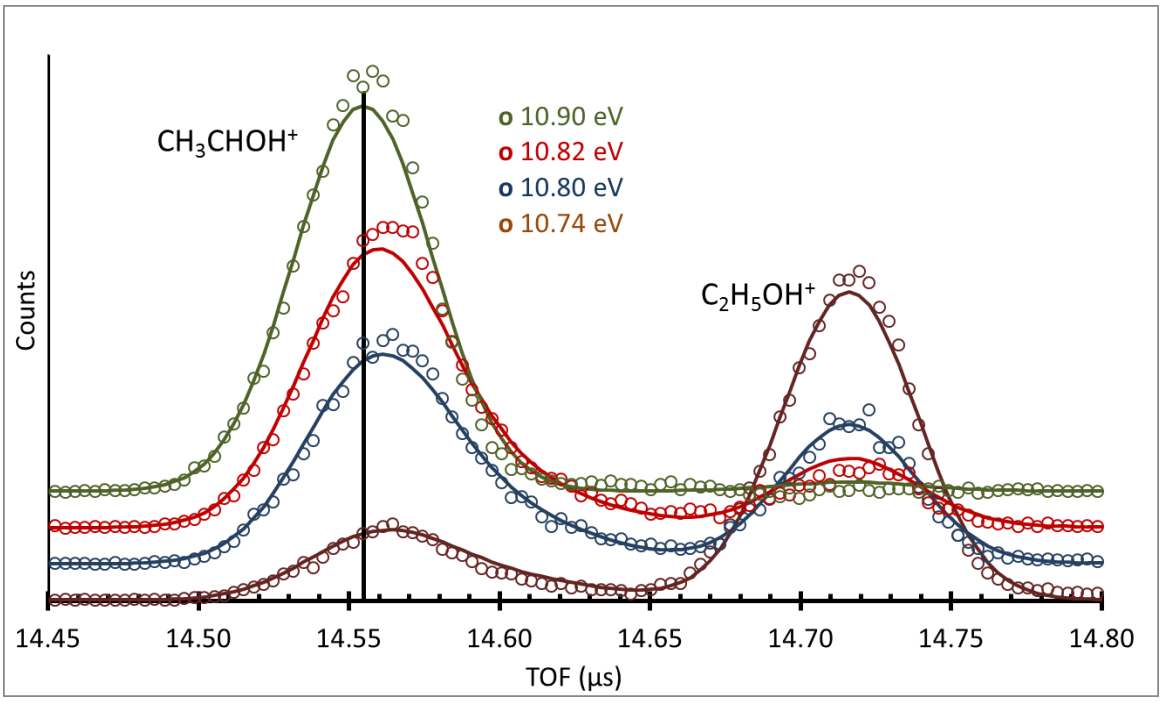

Figure 10. TOF distribution for H loss from energy selected ethanol ions, $C_2H_5OH^+$, at selected energies. Points are experimental results, while the solid lines are the modeled results using the PEPICO modeling program. The vertical line at 14.555 μs corresponds to the TOF peak center of rapidly dissociated product ions. Figure adapted with permission from the PCCP Owner Societies from Bodi et al.[98]

establish the true 0 K onset for H loss from ethanol to be 10.810 eV

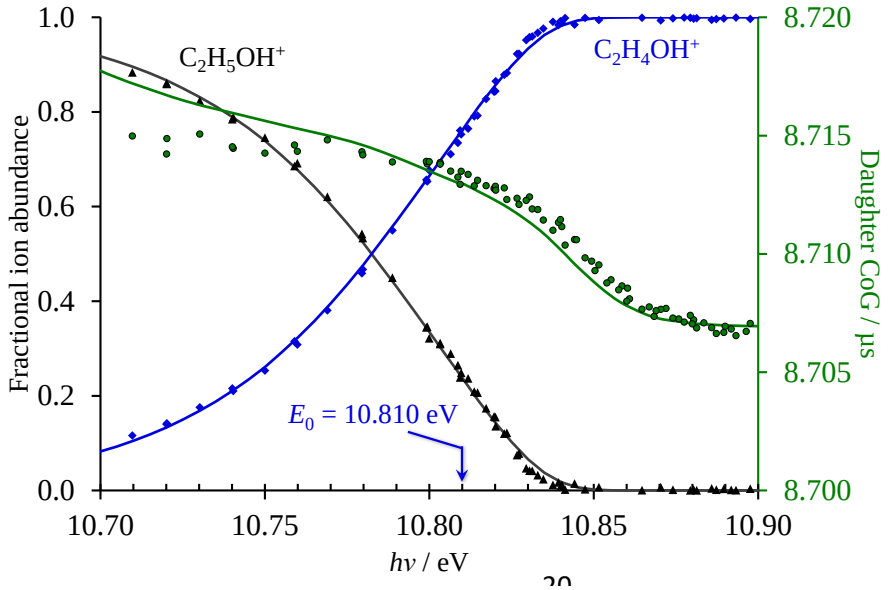

Figure 11. The breakdown diagram for H loss from the ethanol ion, $C_2H_5OH^+$. The green points and the line through them refer to the daughter ion center of gravity (CoG) which shifts to lower TOF as the ion internal energy increases, eventually reaching its limiting value just below 10.90 eV where the reaction is fast. Reproduced from Bodi et al., Ref. 98 with permission from the PCCP Owner Societies.

The extraction of dissociation rate constants from such data is not trivial because it involves extensive data analysis that takes into account the thermal energy distribution of the sample, a model for the dissociation rate as a function of the ion internal energy (e.g. RRKM theory), as well as the energies and vibrational frequencies of the molecular ion and transition state. A PEPICO modeling program that accomplishes all this is available for general use.[102]

4. **Advantages and disadvantages in the use of molecular beam and thermal sample sources**

In both threshold photoelectron and electron ion coincidence studies, the major advantage in the use of a molecular beam source is that the sample is cooled so that the thermal energy distribution is narrower. However, this depends very much on whether the beam is pulsed or continuous. Whereas the vibrational temperatures of pulsed molecular beams have been studied, for instance, by the observation of hot bands and found to be quite low, the cooling afforded by a continuous molecular beam is generally far less efficient because of the much lower gas density in the expansion nozzle.[103] In fact, it is not even evident that the vibrational energy distribution can be characterized by a single temperature. Recently, Brechignac et al.[104] reported on the jet cooling of coronene from a nozzle heated to 640 K and estimated from TOF peak widths that the translational temperature in the beam was 120 K. On the other hand, TPES simulations of hot bands suggested vibrational temperatures for the low frequency modes that ranged between 200 and 350 K. Even rotational temperatures are difficult to cool in molecular beams, Jacovella *et al*.[105] finding that a free jet from a room temperature propyne source cooled the rotations to only 100 K. For many experiments it may therefore be better to operate with a known equilibrium temperature of 300 K than an unknown molecular beam vibrational temperature. Alternatively, it is possible to use a thermally cooled source as demonstrated by Borkar and Sztaray.[106] By circulating a coolant through the ionization region, they were able to cool the ethyl

bromide sample down to -60 °C, thereby considerably narrowing the ro-vibrational energy distribution as shown in Figure 12. Breakdown diagrams for the dissociative photoionization of ethyl bromide are

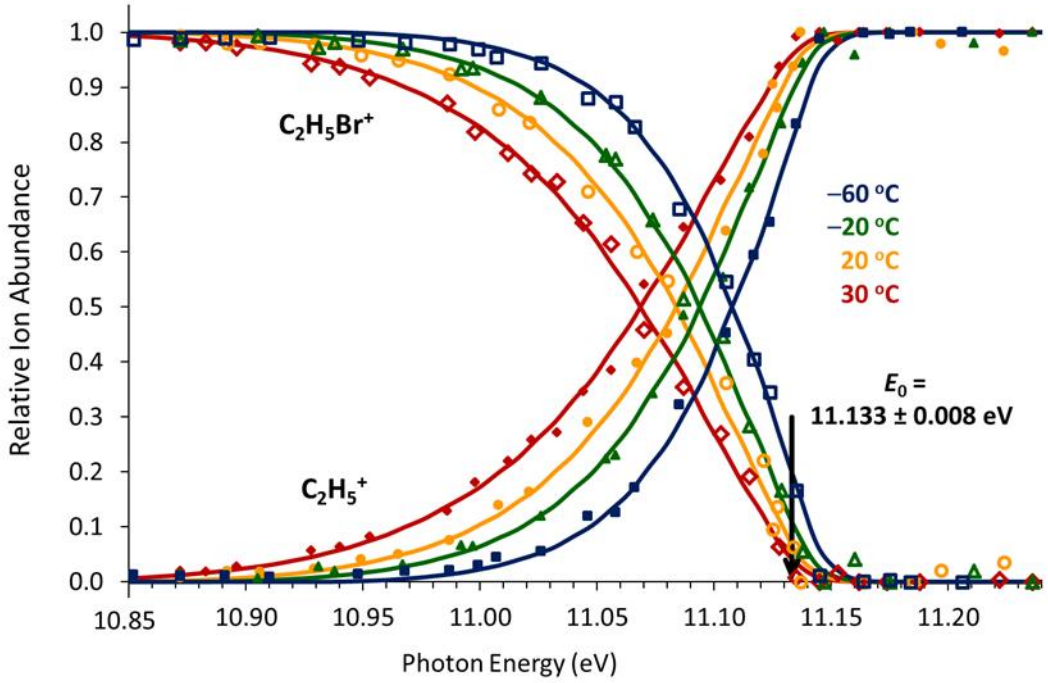

Figure 12. TPEPICO Breakdown diagrams for Br loss from $C_2H_5Br^+$ ions as a function of the source temperature. The solid lines through the experimental points are obtained by assuming a dissociation limit of 11.133 eV and varying only the temperature. Taken from Borkar and Sztáray[106]

shown in Figure 12 at a number of temperatures between -60 and 30 °C (or 213 to 303 K).

A second problem with molecular beam cooling is that these sources often generate large numbers of clusters, which when photoionized generate a mixture of cluster ions, including dissociatively ionized species. It is thus not always easy to distinguish an ion formed by direct ionization [$AB + h\nu \rightarrow AB^+ + e^-$] from one formed by dissociative photoionization [$(AB)_2 + h\nu \rightarrow AB^+ + AB + e^-$]. As shown for the case of the CH_3I photoionization, this ambiguity in the origin of an AB^+ ion peak can lead to significant problems in assigning onset energies.[50] However, the use of time of flight peak widths or ion imaging can

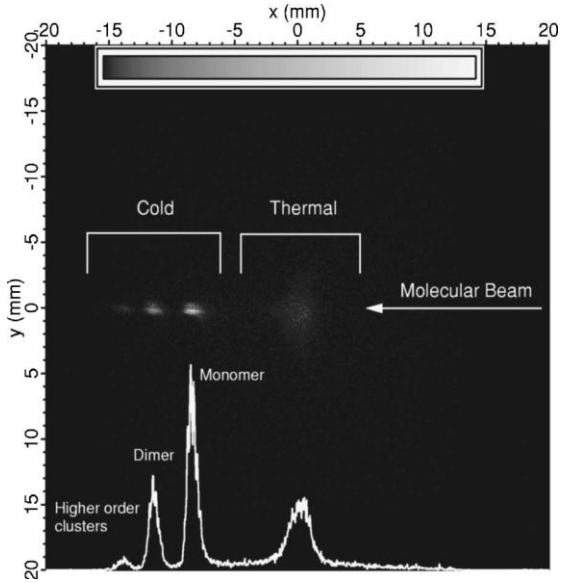

Figure 13. Image of camphor ions originating from the photoionization of a He seeded camphor beam. The diffuse thermal signal in the center exhibits an isotropic translational energy distribution, while the cold ions are displaced because they exited the acceleration region with the velocity of the He beam directed perpendicular to the extraction axis. Reproduced with permission from Nahon et al.[109]

overcome some of the problems associated with the use of molecular beams.[107-109] As shown in Figure 13, the ion imaging approach is particularly powerful. In this experiment, Nahon et al.[109] expanded a beam of He over a heated oven containing the low volatile camphor molecule (MW = 152 g mol^{-1}). The thermal sample that invariably persists in a singly skimmed molecular beam has a room temperature isotropic translational energy distribution and appears as a diffuse spot in the middle of the imaging plate. However, a seeded beam of camphor in a large excess of He assumes the velocity of the He atom beam, in which the full gas enthalpy of 2.5RT is converted into translational energy of the molecular beam. This velocity, directed perpendicular to the extraction axis, is given by $u= (5RT/M_{He})^{1/2}$, where T is the temperature of the heated oven. This large increase in the speed of the camphor molecules not only separates the camphor monomer from the thermal background, but also from the even higher mass dimers and trimers.

The velocity of the He beam is such that the instrument needs to be designed to ensure that the ions are not displaced so much that they fail to hit the imaging plate. The use of Ar as an expansion gas avoids such problems, but is less effective in separating the different peaks. The other difference between Ar and He as expansion gases is that Ar in general is more effective in cooling the internal modes of the seeded molecule. There are important differences in the internal energies of the various peaks in Figure 13. The broad thermal peak, consisting of camphor monomer ions, clearly has the temperature of the ion source which is probably close to room temperature because these molecules have bounced off the source walls. The monomer in the molecular beam has an internal temperature considerably less than the thermal ions, but as mentioned before, its precise temperature is not known. Finally, the weakly bound cluster ion peaks necessarily correspond to ions that are very cold, because the warm clusters would have dissociated.

Unlike the vibrational energy which is uncertain in continuous molecular beams, the translational energy distribution in the direction of the ion TOF axis is very narrow and can readily be measured from the width of the TOF peak of a parent ion. A translational temperature of 5 K was reported by Booze and Baer[107] in the continuous expansion of acetylene, which narrows the TOF peak by a factor of *ca.*eight relative to a 300 K source, thereby greatly increasing the mass resolution. A side benefit is that any broad peaks in the spectrum can be identified as daughter ions due to translational energy release in the dissociation process. Tang et al.[110] recently demonstrated that the use of two skimmers greatly reduces the thermal background in the molecular beam without significantly reducing the signal level. That is, the diffuse peak in Figure 13 can essentially be eliminated.

In conclusion, there are advantages and disadvantages in the use of molecular beams and thermal sources for coincidence experiments involving ion dissociation, and the former are not the universal solution that was perhaps believed when they were first introduced about thirty years ago.

5. Coincidence Studies with imaged electrons and ions

So far, we have discussed imaging primarily with respect to the focusing of threshold electrons from an extended source onto the center of an imaging plate detector or an aperture followed by a channeltron detector. This yields the highest ion internal energy resolution because the threshold electrons can be detected with excellent (sub meV) resolution. However, there are some significant advantages in using the full information on the electron imaging detector, as well as in imaging ion velocities. The actual experiment of imaging both electrons and ions is not too difficult to carry out, and several approaches

and applications at various synchrotron facilities have been reported.[110-113] However, the data analysis can be quite involved.

In both electron and ion imaging studies, the particles hit the imaging detector as concentric rings with radii that are proportional to the electron or ion velocities perpendicular to the extraction axis. Thus the distribution of ejection angles is mapped into a continuous distribution of electron and ion signals on the detector. However, the information in the electron and ion images differ in one important respect which is that we have no useful time of flight information about the electrons that could be used to determine the energy of the electron. Aside from the difficulty in getting a "start" signal, the dispersion of electron arrival times is too small to permit extraction of electron velocity information. This is because, unlike the low extraction field electron TOF experiment shown in Figure 3, imaging studies utilize extraction fields that are typically two orders of magnitude higher than those used for the data in Figure 3. On the other hand, when collecting fragment ions with significant translational energy due to the kinetic energy release in the dissociation, we can obtain their arrival time which provides information about their initial forward or backward velocities, thus complementing the information on the image. That is, we obtain information about the ion velocity perpendicular to the extraction axis from the imaging plate and information about the velocity along the extraction axis from the TOF, thereby providing us with both the total translational energy as well as its angle of ejection.

The extraction of a photoelectron spectrum from an imaging plate thus requires a real deconvolution, involving some assumptions, while similar information about ions can be obtained directly. We now consider the advantages and difficulties encountered in the various types of imaging PEPICO experiments.

(Andras' suggestion for these last two paragraphs) In both electron and ion imaging studies, the particles hit the imaging detector at radii that are proportional to the electron or ion velocities perpendicular to the extraction axis times their mass. Thus the distribution of ejection angles is mapped into a continuous distribution of electron and ion signals on the detector as a function of radius. However, the information in the electron and ion images differ in one important respect, which is that we have no useful time-of-flight information about the electrons to determine the energy of each detected electron. Aside from the difficulty in getting a "start" signal to reference the electron TOF to, the dispersion of electron arrival times is too small to permit extraction of electron velocity information. This is because, unlike the low extraction field electron TOF experiment shown in Figure 3, imaging studies utilize extraction fields that are 2 orders of magnitude higher than those used for the data in Figure 3. On the other hand, there is a dichotomy between setting up ion optics for ion mass resolution, *i.e.,* space focusing conditions to obtain the narrowest possible TOF peak width, and using the ion arrival time to learn about its initial forward or backward velocity, thus complementing the momentum information of the ion hit position. That is, by sacrificing mass resolution, we can obtain information about the velocity perpendicular to the extraction axis from the imaging plate and information about the velocity along the extraction axis from the TOF, thereby providing us with both the total ion translational energy as well as its angle of ejection.

The extraction of a photoelectron spectrum from an imaging plate thus requires a real deconvolution, involving some assumptions. Ion 3D momentum imaging or applying slicing is therefore quite appealing, since the kinetic energy and angular distribution of ions can be obtained directly, albeit with some signal

loss in the latter case. The major disadvantage of using the TOF for momentum analysis along the extraction axis is the need for translationally cold sample for mass information. Sharp m/z peaks are also advantageous for background subtraction and improve the dynamic range of the experiment. Therefore, space focusing with or without velocity map imaging the ions is highly beneficial in analytical applications, or when the fragmentation pattern is not *per se* known and H losses are possible, or when the sample source is inherently hot, for example, in pyrolysis experiments. However, while the reconstruction of the one-dimensional spectrum based on velocity map images is routinely possible, the inversion of two velocity map images recorded in delayed coincidence to obtain the energy correlation diagram is still an outstanding issue, which limits the application of double velocity map imaging apparatuses.

5.1 Threshold electron detection in coincidence with imaged ion velocities

There are two major advantages of imaging ions by velocity focusing optics. One of these has already been mentioned when the sample is in the form of a molecular beam (see Figure 13), and the ion image can be used to separate thermal background signal as well as clusters from the monomer beam signal. The other advantage is the ability to measure the release of translational energy upon ion dissociation. Large ions that dissociate statistically from their ground electronic state generally have broad distributions of translational energy that peak close to zero energy, which are understood in terms of well-established statistical models.[114,115] On the other hand, some large ions have been found to dissociate directly from excited and repulsive electronic energy states that result in the release of relatively large translational energy.[78,116,117] In contrast to large ions, di- or tri-atomic ions with their sparse vibrational levels do not dissociate statistically. Instead, they dissociate to products formed in specific electronic and/or vibrational levels whose identity can be determined from the measured translational energies. The translational energy release in the dissociation of small ions by ion imaging has been used to great advantage mostly by the group of Zhou.[113,117,118]

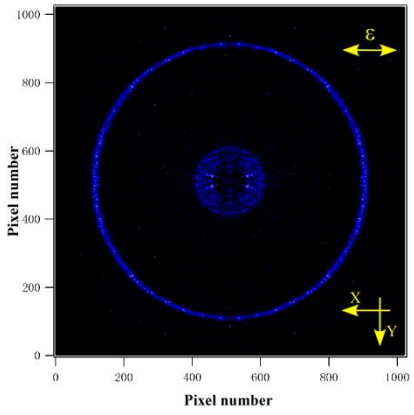

Figure 14. Time sliced velocity map images of the dissociation of O_2^+ at 20.817 eV. Two overlapping states [$B^2\Sigma_g^-$ (v=4) and $^2\Sigma_u^-$ (v=5)] contribute to the large translational energy of the ground state products, O^+ (^4S) + O(^3P), whereas the small energy release associated with the excited state products, O^+(^4S) + O(^1D) arise from the $^2\Sigma_u$(v=5) ion state, exclusively. The diffuse appearance of the inner ring is a result of the difficulty in slicing the image with a 60 ns gate. Figure reproduced with permission from Tang et al.[119]

The analysis of the ion images was greatly simplified by the application of time sliced imaging in which only the ions ejected perpendicular to the extraction axis are collected by a multichannel plate detector followed by a phosphor imaging system. Consider the dissociation of a diatomic ion to a single dissociation channel with a single translational energy. The ion cloud dissociates into a sphere with equal intensities for the case of an isotropic dissociation or with angular variations in the case of non-

isotropic dissociation. In any case, those ions ejected in the forward and backward parallel direction relative to the ion extraction field will arrive, respectively, before and after the ions that are ejected perpendicular to this axis. If all ions were collected on the imaging plate, the image would look much like one of the basis functions in Figure 6. However, by gating the ion signal so that only those ions ejected perpendicular to the extraction axis are collected, it is possible to have the signal from a single dissociation reaction appear only as a narrow ring as shown in Figure 14. The time slicing approach is particularly useful when a phosphor imaging system is employed because there is no intrinsic ion arrival time information available to permit a proper inversion of the ion image. The example in Fig. 14 is for the case of two O_2^+ ion states that by chance overlap at an energy of 10.817 eV.[119] These are the optically active $B^2\Sigma_g^-$ (v=4) and the $^2\Sigma_u^-$ (v=5) states, the latter being optically inaccessible and thus much weaker. This result, as well as data at other energies, show that the two electronic states dissociate to the ground state, O^+ (^4S) + O(^3P), while the ungerade state dissociates only to the excited products.

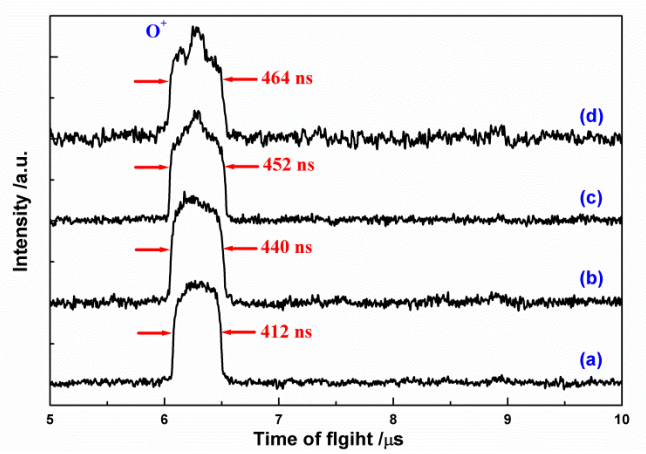

Figure 15 Time of flight data for the dissociative photoionization of O2 at the following photon energies: (a) 20.353 eV, (b) 20.727 eV, (c) 10.817 eV, (d) 20.897 eV. Figure reproduced with permission from Tang et al.[119]

It is of some interest to compare the VMI image of Figure 14 with similar data obtained by TOF. That is, instead of displaying the dispersion of the fragment ion kinetic energies perpendicular to the ion flight direction (Figure 14), it is also possible, and indeed historically more common, to display the dispersion along the ion flight direction as TOF peak broadenings. Figure 15c shows the ion O^+ TOF at a photon energy of 20.817 eV (same as in Figure 14). The broad rectangular peak corresponds to the large energy release while the small top part is due to the low energy release that corresponds to the production of the excited dissociation products. The time sliced data in Figure 14 corresponds to a thin time slice centered on the peak at about 6.3 μs. Finally, it is worth noting that the time slice method works best for simple ions that dissociate to products that have large differences in mass because the gating pulse is not sufficiently precise to permit resolving product ions that differ by only a few mass units.

The measurement of fragment ion velocities from ion images for polyatomic ions was reported by Tang et al.,[120] in which the fragment ion translational energies have been used to provide new information about the CH_3Cl and CH_3F photoelectron spectra. The results are most dramatic for CH_3Cl in which the excited *A* $^2A_1$ and *B* ^2E ion states are overlapped, so that the adiabatic onset for the *B* state is not resolved. However, as Tang et al.[121] showed, the *A* state of the CH_3Cl^+ ion is dissociative producing high kinetic energy CH_3^+ fragment ions, while the *B* state is bound and apparently internally converts to the ground electronic state prior to statistical dissociation. Thus, by measuring the photoelectron spectrum

in coincidence with low energy CH_3^+ ions, it was possible to suppress the $A\ ^2A_1$ state, thereby clearly revealing the adiabatic onset for the CH_3Cl^+ $B\ ^2E$ state.

5.2 Slow Photoelectron spectroscopy (SPES) using electrons dispersed on an image

A simple approach to using, at least, partial information contained in the dispersed electron image for threshold electron spectroscopy of anion photodetachment processes was introduced some years ago by Neumark and co-workers,[122] and adapted for synchrotron radiation studies by Poisson and Hochlaf at the Soleil synchrotron in France.[123,124] Poully et al.[124] applied this to the molecule, 2-pyridone. They collected full images of the electrons in coincidence with the parent ion as they scanned the photon energy from below the IE through the vibrational modes of the 2-pyridone cation. Using an Abel transformation,[125] they then transformed the 2-D electron images to photoelectron spectra at each photon energy. These data are shown in a single 2-D plot in Figure 16, in which the photon and electron energies are plotted on the x and y-axes, respectively, and the electron intensities are on the third axes, color coded with red being the most intense and black being zero. Traditional photoelectron spectra (PES) at selected photon energies could be obtained by vertical cuts. The traditional threshold photoelectron spectrum (TPES) is obtained by scanning the electron intensities over a narrow range of electron energies, say 0-1 meV, as a function of the photon energy. However, similar constant electron energy spectra could be obtained at other electron energies; that is, the threshold electron spectrum from Figure 16 is repeated at higher electron energies, albeit with a shifted onset. Although the energy resolution decreases with the electron energies that are being scanned, it is evident that it is quite adequate over a significant range of energies, and that this multiplicity of information can be used to improve the signal-to-noise ratio without a major penalty in the resolution. In their study of the 2-pyridone molecule, Poully et al.[124] combined the electron spectra up to 75 meV, calling this Slow Photoelectron Spectroscopy (SPES) to distinguish it from the related TPES.

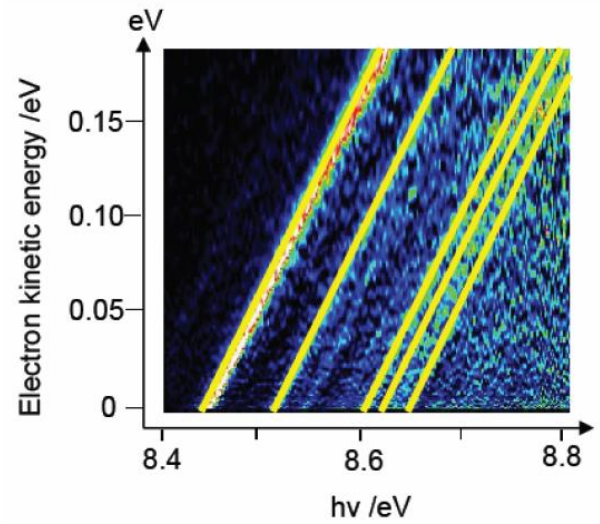

Figure 16: 2D spectrum representing the kinetic energy of the photoelectrons in the range 0-180 meV as a function of the photon energy in the 8.4−8.8 eV range. The intensity of the photoelectron signal increases from blue to red, black representing zero. The energy of the photoelectrons increases linearly with the photon energy. Taken with permission from the PCCP Owner Societies from Poully et al.[123]

The resulting SPES of 2-Pyridone, plotted in Figure 17, shows not only the 2-pyridone spectrum with its IE at 8.44 eV, but also the 2-hydroxypyridine tautomer at a slightly higher IE of 8.92 eV. The solid

pyridine sample was heated in an oven to 160 ^{o}C and then cooled in a He seeded molecular beam. As shown by the inset, the ground state peak width is quite narrow, 9 meV, which can be attributed to efficient cooling of the sample rotational modes. The high quality of the SPES in Figure 17 demonstrates the utility in using as much of the imaging plate signal as possible to improve the signal to noise and/or to reduce the time necessary to collect the spectrum.

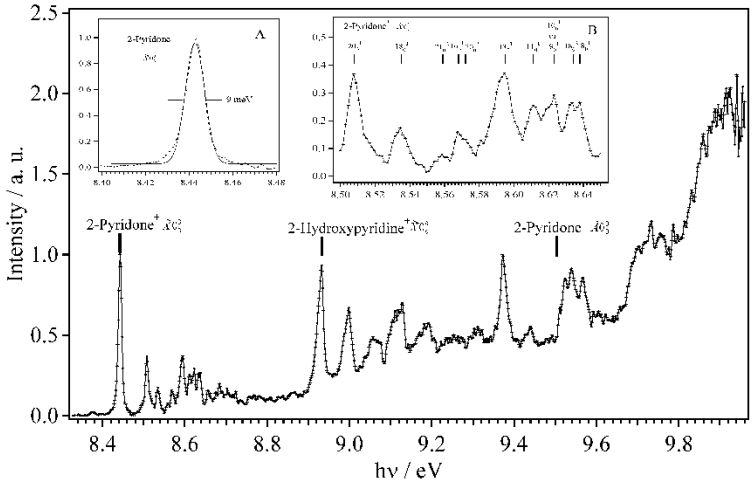

Figure 17. Slow photelectron spectrum (SPES) of 2-Pyridone and its conformer, 2-hydroxypyridine. The insets are expanded scans of the ground state, showing a peak width of 9 meV, and the resolved vibrational levels of the Pyridone ion. The hydroxypyridine spectrum begins at 8.85 eV. Taken with permission from the PCCP Owner Societies from Poully et al.[123]

5.3 Ion detection in coincidence with all electrons dispersed on an image

The imaging detector that focuses threshold electrons in the center of the detector also focuses the energetic electrons in rings whose radii are proportional to their velocity in the perpendicular direction. Thus if ions are collected in coincidence with electrons from the full image at a fixed photon energy, hν, coincidence data can be collected simultaneously at all energies from the ionization energy (IE) up to the maximum electron energy (hν-IE). This can be particularly advantageous for low density samples such as non-volatile compounds or transient species created in discharges, pyrolysis, or flame studies.

As described at the start of Section 5, the fundamental problem is that electrons of a given energy are ejected in a distribution of angles and it is only the velocity projection perpendicular to the extraction axis that determines the radial position of the signal on the imaging detector. That is, the three dimensional ejection (angle and energy) of the electron is projected onto a two dimensional detector. As a result, there is no way of knowing the electron energy on the basis of its position on the detector. A number of methods have been reported for extracting the full 3-D image,[125-129] but all of them involve some assumptions. A recent approach, especially suitable for coincidence experiments, involves the forward convolution of a series of electron basis functions with the photoelectron spectrum from zero to the maximum electron energy.[130] The basis functions, $B(r,E_{el})$, are the intensities of the electron signal from a series of single energy (E_{el}) electrons assumed to have been isotropically ejected, which is often the case for intermediate to large molecules. The basis functions are equally spaced in electron velocities, *i.e*. in equal increments of $k(E_{el})^{1/2}$, which means equally spaced radii on the imaging plate. The value of k is a constant that is chosen as a compromise between optimum energy resolution and signal to noise. The full image of the photoelectrons, PE(r), at a fixed photon energy, hν, can then be expressed as:

$$C(E_{el})\otimes B(r,E_{el}) = PE(r) \qquad (16)$$

where $C(E_{el})$ is the column matrix of the coefficients (*i.e.* the photoelectron spectrum), $B(r,E_{el})$ is the calculated 2-dimensional matrix of the basis functions for the single electron energy distributions, and PE(r) is the experimental image of all the electron energies from zero up to (hν-IE). The full electron image (coincidence signal with parent and all fragment ions) can then readily be inverted using linear algebra methods to obtain a series of coefficients for the basis functions, which constitute the photoelectron spectrum. If the basis functions are too closely spaced, some coefficients can be negative.

With the coefficients of the basis function in hand, it is then possible to model the parent and fragment ion intensities as a function of the electron energies to obtain the breakdown diagram. A test of this procedure was carried out for three isomers of bromobutyne, C_4H_5Br, by collecting the high resolution breakdown diagram using just threshold electrons, as well as the imaging approach outlined here.[130] Figure 18a on the left shows the breakdown diagrams for one of the isomers obtained by the traditional

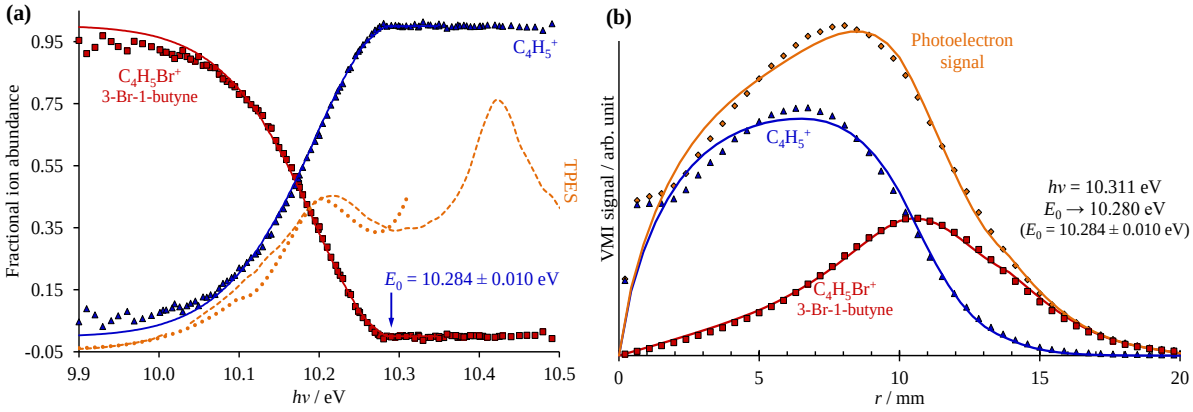

Figure 18. The two figures show the breakdown diagrams for 3-Br-1-butyne. On the left is the traditional breakdown diagram (ions as a function of the photon energy) obtained by ion threshold coincidence (TPEPICO) along with the high resolution TPES. On the right are the data obtained by collecting all electrons in coincidence with the ions at a photon energy of 10.311 eV, which display the ions as a function of the radial electron signal. The 0 K dissociation onset energies obtained from the two methods are 10.284 ± 0.010 eV and 10.280 eV, which are in excellent agreement. Adapted with permission from the PCCP Owner Societies from [130].

TPEPICO method in which the data are collected at a series of photon energies. Figure 18b on the right shows the breakdown diagram obtained at a single photon energy of 10.311 eV but using the full electron image which contains electrons with energy from zero to the maximum of (hν-IE). The latter figure displays the parent and fragment ions as a function of the electron signal at various radii. The two plots look very different because the TPEPICO data on the left display the ions collected in coincidence with strictly zero energy electrons so that the only broadening of the breakdown diagram is a result of the thermal energy distribution of the ions. On the other hand, the imaging PEPICO (iPEPICO) results on the right are further broadened by the distribution of electrons over the whole imaging plate. In Figure 18a, the dotted line is the PES at 10.311 eV, which matches the TPES reasonably well. In summary, the VMI/PEPICO data in Fig. 18b were obtained by collecting the full electron image in coincidence with all ions at two photon energies with acquisition times of about 1000 s each. This is ten times shorter than the acquisition time associated with the TPEPICO data in Fig.18a, which were collected at about 100 separate photon energies for 200 s each.

Photoionization has long been recognized as a very precise and information rich tool for identifying unknown reaction products, because it provides not just the mass of the unknown ion but also its ionization energy. Photoionization has thus been used as the preferred analytical tool for detecting the products of radical – molecule reactions in gaseous flow reactors and the products of controlled flame studies.[131-133] These studies have been carried out by scanning the photoionization mass spectrum as a function of the photon energy using synchrotron radiation, which is the only tunable photon source with sufficient intensity to provide sufficient signal. However, it has become clear that as the systems being investigated become more complex and the products more numerous, the mass and ionization energy is not sufficient to identify some products, especially because the photoionization scan only provides the integral of signal from all ions as the photon energy is increased. Thus, in recent years, the application of PEPICO (which is the derivative of the photoionization signal and thus provides more detailed information) to these experiments has become very attractive.

A first attempt to determine quantitatively the composition of an isomer mixture using PEPICO with the full PES on an imaging plate was carried out at the Swiss Light Source (SLS) synchrotron. A mixture of stable molecules, namely C_4H_6 (butadiene and 2-butyne) and C_5H_8 (cyclopentene, isoprene, 1-pentyne, and 1,4-pendadiene) was photoionized at a fixed photon energy and the full PES ranging from 0 to 0.8 eV collected on the imaging plate.[134] Velocity map images of electrons from the pure compounds were also collected at the same photon energy. Linear combinations of these images were then used to fit the electron image of the mixture. Because the images themselves were used in the fitting process, this procedure did not involve an inversion of the image, thereby avoiding the inevitable introduction of noise associated with such inversions. It is evident that the use of images for the pure stable compounds obtained on the same instrument under identical experimental conditions is a very simple and robust approach.

The first study that applied iPEPICO to obtain the photoelectron spectra of products produced in a flame experiment was reported by Osswald et al.[135] In this study of an isobutane-oxygen flame, threshold PES of three C_4H_9 radical isomers were collected with a resolution of 15 meV, and it was clearly possible to distinguish t-butyl, 2-butyl, and two iso-butyl products by their PES. However, because only threshold electrons were collected, it was necessary to scan the photon energy to get a complete TPES. The vast improvement in identifying products by their PES compared to a simple photoion scan is clear from Figure 19. The difficulty in identifying most free radicals by PIE is that the large geometry change between radicals and their ions results in broad PES, which makes their identification nearly impossible by PIE. However, assigning structures to the PES is also not trivial either because the published radical PES vary greatly in their peak shape in part because of the difficulty in controlling the temperature of the radicals which are generally produced by discharges or flash pyrolysis. Although the signal to noise in the experimental spectrum is not excellent, it is possible to confirm that the two major radicals produced are the t-butyl and the i-butyl radicals with vertical IEs at 6.59 and 8.31 eV.

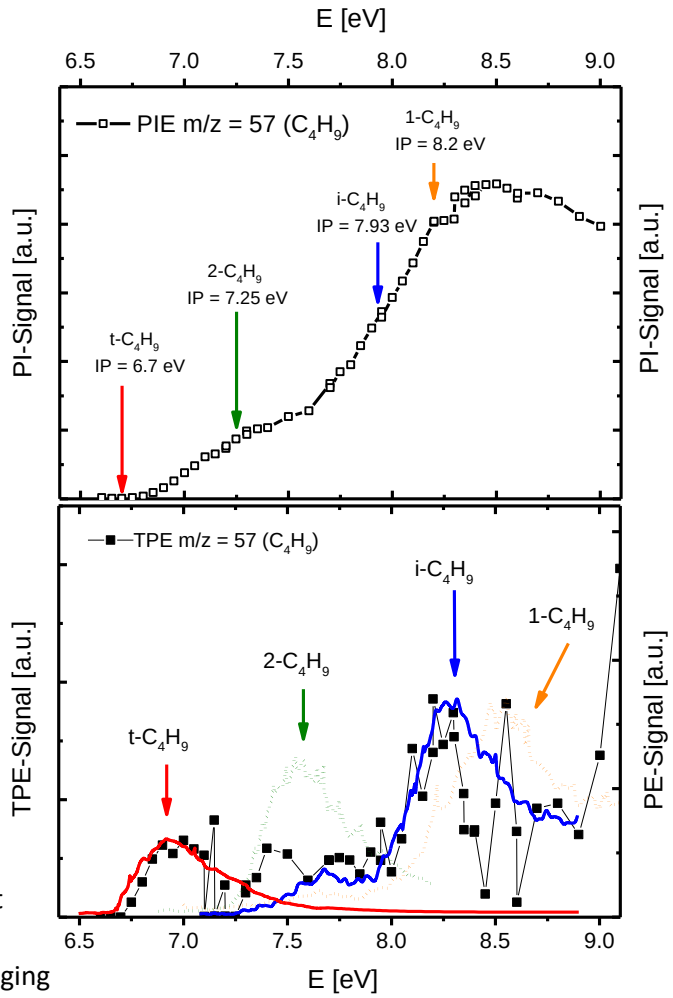

Figure 19 Top panel: Photoionization efficiency (PIE) scan of m/z 57 products from a fuel rich isobutene combustion flame. The arrows indicate the "known" adiabatic ionization energies of the four radicals.
Bottom panel: The threshold PES of the reaction mixture (black points and line). The electron resolution was 15 meV and the acquisition time was 10 min per data point. The coloured lines are the known PES for the four butyl isomers. Taken with permission from Osswald et al.[135]

The first full imaging diagnostic PEPICO experiments of flame products have been carried out at the SOLEIL synchrotron.[136,137] Felsmann et al.[136] investigated the products in laminar premixed flames that generated a broad array of product species, some of which consisted of equal mass isotopomers as well as isomers of the same molecular formula. The full photoelectron spectra at selected photon energies were collected in coincidence with ions of varying masses, an example of which is shown in Figure 20. Data acquisition for this spectrum with good resolution and signal to noise was 1 hour. The photon energy of 9.94 eV was lower than the IE (10.15 eV) of the methyl propionate fuel, thereby avoiding not only photoelectrons from the fuel, but also fragment ions from the methyl propionate ion dissociation. Unfortunately, sample spectra of the pure compounds with similar resolution in the same apparatus

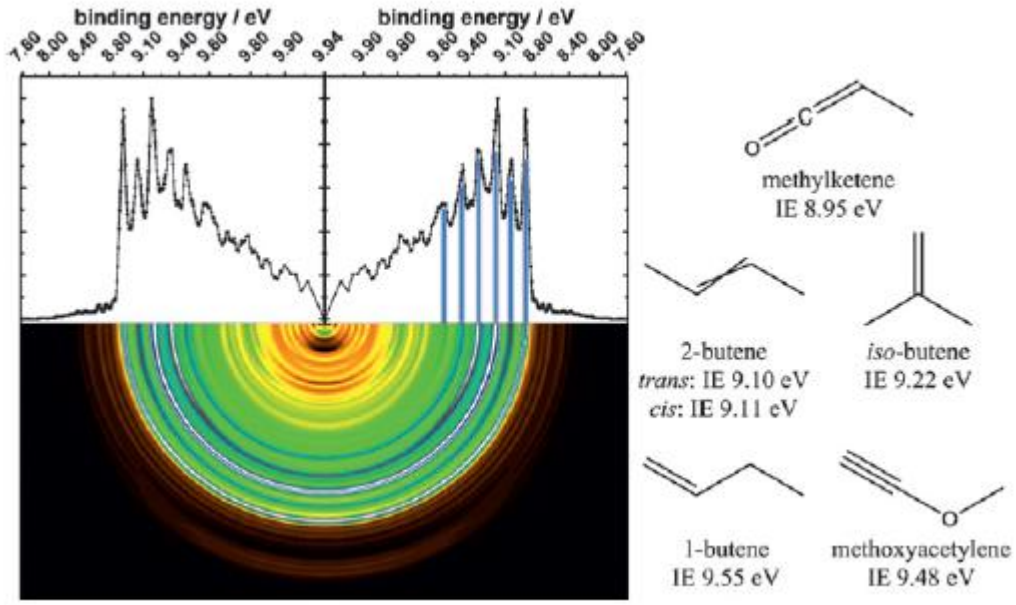

Figure 20: Photoelectron spectrum at 9.94 eV photon energy collected in coincidence with ions of mass 56 recorded in a methyl propionate / oxygen flame at a fixed height above the flame burner. The upper 2-D spectrum is the reconstructed PES of the lower image using the pBasex inversion procedure. At the right are various isomers of mass 56 that can contribute to the total signal. Taken with permission from the PCCP Owner Societies from Felsmann et al.[136]

were not collected so that the authors relied on lower resolution literature spectra. This required degrading the resolution of the PES in Figure 20. In addition, rather than convoluting the known spectra to minimize the global error, the data were fitted by a sequential subtraction approach beginning with the lowest IE isomer (methylketene). This resulted in an error propagation that accumulated the error in the higher IE compounds.

In addition to identifying the product species, it is equally important to obtain relative abundances, or mole fractions, of the various combustion products. The use of fixed photon energy PES is particularly useful for this purpose, especially if the pure compounds are obtained at the same photon energy. Krueger et al.[137] have taken advantage of this approach in establishing the mole fractions of methyl radical and propyne products in an ethane-oxygen flame.

These initial results point out the following important considerations:

1. PE spectra from images should be collected in order to maximimze the signal to noise as well as the resolution of the data. In addition, as pointed out by Krueger et al.[137] and Felsmann et al.[136] the use of a fixed photon energy greatly simplifies the determination of quantitative product yields because all data are collected at a single photon energy, thereby requiring only a single calibration of signal vs yield.
2. Whenever possible, the PES of pure compounds should be obtained with the same instrument under identical conditions. They can then be used to deconvolute the composite spectrum, using a least squares procedure to distribute the errors among the various components.

3. The question of image reconstruction should be considered carefully because if the PES of the pure compounds are obtained as images, there may not be any advantage in working with reconstructed images rather than the image itself.

5.4 False coincidence suppression by ion imaging

As pointed out in the discussion of coincidence statistics, false coincidences are an unavoidable consequence of coincidence studies. While their presence in low flux experiments is normally not detrimental to the overall quality of the data, the false coincidence background becomes increasingly important as the total ion count rate increases. As demonstrated in Eq. 11, this is not deleterious when we are dealing with a simple mass spectrum that consists of a few mass peaks of similar intensities. However, if the coincidence mass spectrum contains very low intensity peaks that are of interest, the false coincidence background generated by the dominant peaks will seriously hinder the analysis of the weak peaks because it will introduce so much noise that the peaks may not be visible. Examples where this could be a problem include the detection of free radicals and other intermediate species in flame studies. If the ionization energy of the minor species is lower than that of the fuel, it is possible to choose a photon energy that is above the free radical IE but below the IE of the fuel, thereby avoiding the massive signal of the fuel. This is precisely the situation in the case of the oxygen-isobutene flame experiment shown in Figure 19, in which the isobutene IE of 10.68 eV is well above the IEs of the free radicals. However, there are other radicals and intermediates whose IEs are not so low, as for example, the OH radical (13.0 eV). In addition, it is often of interest to determine the relative amounts of the all the species in the flame, which requires a very large dynamic range of sensitivities which is limited by the false coincidence background.

A very exciting and novel use of ion imaging has recently been reported by Osborn et al.[138] in which all ions are deflected in two dimensions by periodic triangular deflection voltages applied to an einzel lens-like deflector assembly through which the ions pass. As shown in Figure 21, the first and third cylindrical elements of the lens are at the flight tube voltage, while the central cylinder is divided into four sections to which the 200 V triangular waveform pulses are applied. The output V_{+x}, V_{-x}, and V_{+y}, V_{-y} voltages pairs are AC-coupled to the flight tube high voltage and the full ±200V swing results in an ion deflection of about ±20 mm on the ion imaging detector. The frequencies of the triangular deflection voltages (adjustable between 20 and 100 kHz) are slightly mismatched between the *x* and *y* directions so that the ions are spread out in a 2-dimensional geometric pattern on the imaging plate, as shown in Figure 20 for the case of Ar^+ ions.

Thus, instead of all ions (real and false coincidences) appearing at only a single location on the imaging plate, this ion deflection technique disperses the ions so that the ion arrival time and place are calculably connected for a true coincidence, while the false coincidences appear at locations that are inconsistent with their times of flight. Osborn et al.[138] showed that, for the case of a photoionized Ar molecular beam that consists primarily of Ar^+ ions, along with oligomers of rapidly decreasingly intensity, it is possible to reduce the false coincidence background by two to three orders of magnitude, which permitted the observation of Ar_9^+ ions. This is compared to the normal coincidence spectrum in which the highest observable cluster was the Ar_4^+ ion.

The success of this method to suppress false coincidences depends very much on the VMI ion optics that yield a very small spot (less than one mm in both directions) on the imaging plate detector for the

undeflected ions. The suppression factor for false coincidences is then related to the ratio of the total imaging plate surface area to the ion spot size. According to Furuya and Kimura[139] all Ar_n^+ cluster ions are formed from dissociative photoionization so that their TOF peak width are broadened by the kinetic energy release. However, in the experiment of Osborn et al., this has clearly not hampered the analysis, perhaps because of the high draw-out voltage for the ions which minimized their peak TOF widths and spatial dispersion.

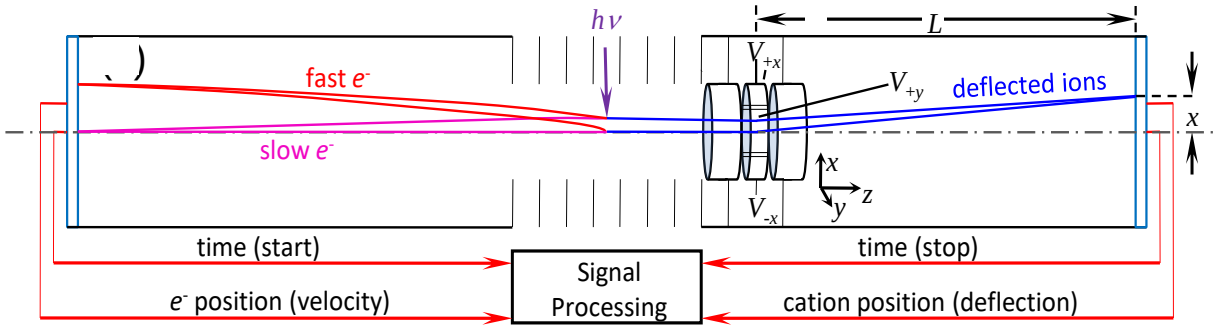

Figure 21 Experimental set up for suppression of false coincidences in high flux photoionization studies. The first part of the ion drift tube consists of an Einzel lens in which the middle element is divided into four sections that can be used to deflect the ions in the ± x and ± y directions, thereby dispersing the real coincident ions into predictable patterns (see Figure 20) on the ion imaging detector. Taken with permission from Osborn et al.[138]

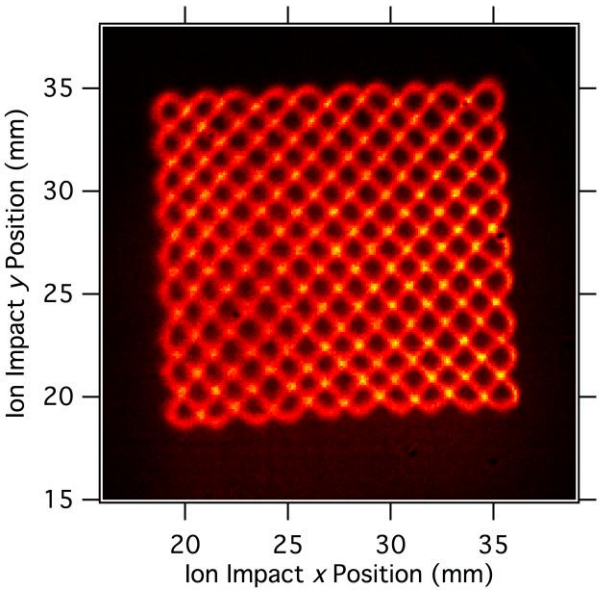

Figure 22 Image of deflected Ar+ ions using the x-y deflection scheme illustrated in Figure 21. Taken with permission from Osborn et al.[138]

6. Conclusions and future directions

This paper has described the history and evolution of both threshold photoelectron spectroscopy and threshold photoelectron photoion coincidence spectroscopy over the last fifty years. Emphasis has been placed on instrumentation and the kinds of scientific problems that can be addressed, not on the detailed spectroscopy of certain molecules. In our opinion, three important advances have expanded greatly the power of the technique, and permitted its implementation in modern synchrotron radiation beamlines. The use of velocity focusing of threshold electrons onto an imaging detector in the 1990s simultaneously improved the sensitivity and electron energy resolution, and facilitated the subtraction of hot electron background in both threshold electron spectroscopy and TPEPICO studies. The development of multi-start multi-stop collection detectors for both electrons and ions in the 2000s permitted the use of the full intensity of modern synchrotron radiation thereby greatly improving the signal-to-noise ratio. Finally, recent developments involving imaging electrons in a range of energies as well as ions onto separate position-sensitive detectors has further improved the collection sensitivity so that low density samples found in a variety of studies can be investigated. It is interesting that while TPEPICO initially was developed using low intensity laboratory light sources, the real power of the method can only be realized when it is coupled to high intensity and high resolution synchrotron radiation sources. As a result, nearly all TPEPICO setups are now located at synchrotron radiation facilities.

The first 50 years of TPEPICO studies have been directed primarily at improving our fundamental understanding of unimolecular dissociation reactions and our ability to extract accurate dissociation energies from the data. As a result, a large fraction of the thermochemistry of ions and free radicals has been established by TPEPICO.[140,141] Such experiments will certainly continue and could in fact be expanded by adapting double imaging experiments to revisit an old field, namely ion-pair formation induced by photons: $ABC + h\nu \rightarrow D^- + E^+$ (+ neutrals). This dissociation path at low energies generally is competitive with other decay channels only below the molecule's first ionization limit, and is thus ideally suited for investigation with vacuum-UV light (ca 6 to 12 eV). The adaption of the electron optics to detect negative ions is straight forward. One of the authors has both studied and reviewed extensively the formation of negative fragment ions from polyatomic molecules by mass spectrometry.[142] In many studies only the anion is detected so that the cation (plus possibly neutrals(s)) has to be inferred/guessed, usually by energetics. However, in polyatomic ion pair formation where both the anion and the cation can be produced in a range of internal vibrational states, it is highly advantageous to detect not only both ions, but also measure their translational energy distributions in order to obtain the full information about the dissociation dynamics. Detection of anions and cations in coincidence, a process usually of low cross section, will also suppress the direct ionization or dissociative ionization reactions $ABC + h\nu \rightarrow ABC^+ + e^-$ or $AB^+ + C + e^-$ which have much higher cross sections. Such studies have in fact been pioneered primarily by Suits and Hepburn,[143] who utilized vacuum UV lasers as the ionization source in order to determine highly accurate electron affinities, as well as for investigating the fundamental dynamics of the ion pair formation process. Recent results on a closely related experiment have been reported from the Elettra synchrotron in Italy using soft X-ray photoexcitation,[144] but it is suggested that the lower-energy vacuum-UV region which is much closer to the ionization energy of the molecule under study, and where the number of possible dissociation channels are much more limited, would be a very profitable area for study.

Although the fundamental studies of photoionization and ion dissociation will no doubt continue, we expect that future advances in the field will almost certainly be driven by the multiplex advantages of imaging detection of electrons and ions. Preliminary studies that are described in this review, carried

out so far mainly at the Soleil, France and Swiss Light Source synchrotrons, have shown that the increased signal levels obtained by using the full information from electron energies dispersed on an imaging detector permit collecting high resolution (sub 10 meV) photoelectron spectra of low density molecules or free radicals. When these are collected in coincidence with mass analyzed ions, it is possible not only to identify reaction products by their photoelectron spectra, but also to obtain quantitative information about the relative concentration of products in a mixture. With the advent of new, more sensitive techniques and false coincidence suppression thereby yielding a 2-3 orders magnitude more dynamic range, PEPICO now also holds the promise of a truly universal and isomer selective gas phase analytical tool.

Acknowledgements : We thank Drs Andras Bödi and Laurent Nahon for a critical reading of the manuscript, as well as Drs Bálint Sztáray, Xiaoguo Zhou, and George King for sending us high resolution copies of their figures.

Reference List

1. Eland, J. H. D. Coincidence studies of multiionized molecules. In *Vacuum Ultraviolet Photoionization and Photodissociation of Molecules and Clusters*, Ng, C. Y., Ed.; World Scientific: Singapore, 1991; pp 297-344.

2. Eland, J. H. D. Photoelectron-photoion coincidence spectroscopy I. Basic principles and theory. *Int. J. Mass Spectrom. Ion. Proc.* **1972,** *8*, 143-151.

3. Eland, J. H. D. Predissociation of N_2O^+ and COS^+ ions studied by photoelectron photoion coincidence spectroscopy. *Int. J. Mass Spectrom. Ion. Proc.* **1973,** *12*, 389-395.

4. Arion, T.; Hergenhahn, U. Coincidence spectroscopy: Past, present and perspectives. *J. Electron Spectrosc. Relat. Phenom.* **2015,** *200*, 222-231.

5. Villarejo, D.; Herm, R. R.; Inghram, M. G. Measurement of threshold electrons in the photoionization of Ar, Kr, and Xe. *J. Chem. Phys.* **1967,** *46*, 4995-4996.

6. Villarejo, D. Measurement of threshold electrons in the photoionization of hydrogen and deuterium. *J. Chem. Phys.* **1968,** *48*, 4014-4026.

7. Baer, T.; Peatman, W. B.; Schlag, E. W. Photoionization resonance studies with a steradiancy analyzer. II. The photoionization of CH_3I. *Chem. Phys. Lett.* **1969,** *4*, 243-247.

8. Peatman, W. B.; Borne, T. B.; Schlag, E. W. Photoionization resonance spectra. I. Nitric oxide and benzene. *Chem. Phys. Lett.* **1969,** *3*, 492-497.

9. Baer, T.; Tsai, B. P. Resonance photoelectron spectroscopy from autoionization states of CH_3I. *J. Electron Spectrosc. Relat. Phenom.* **1973,** *2*, 25-32.

10. Tsai, B. P.; Baer, T.; Horowitz, M. L. A time of flight detection system for near threshold photoelectron spectroscopy. *Rev. Sci. Instrum.* **1974,** *45*, 494-498.

11. Spohr, R.; Guyon, P. M.; Chupka, W. A.; Berkowitz, J. Threshold photoelectron detector for use in the vacuum ultraviolet. *Rev. Sci. Instrum.* **1971,** *42*, 1872-1879.

12. Baer, T.; Squires, L.; Werner, A. S. Collisional dissociation of $CH_2Br_2^+$ in selected internal energy states. *Chem. Phys.* **1974,** *6*, 325-330.

13. Stockbauer, R. A threshold photoelectron photoion coincidence mass spectrometer for measuring ion kinetic energy release on fragmentation. *Int. J. Mass Spectrom. Ion. Phys.* **1977,** *25*, 89-101.

14. Rosenstock, H. M.; Stockbauer, R.; Parr, A. C. Kinetic shift in chlorobenzene ion fragmentation and the heat of formation of the phenyl ion. *J. Chem. Phys.* **1979,** *71*, 3708-3714.

15. Rosenstock, H. M.; Stockbauer, R.; Parr, A. C. Photoelectron-photoion coincidence study of benzonitrile. *J. Chim. Phys.* **1980,** *77*, 745-750.

16. Wiley, W. C.; McLaren, I. H. Time of flight mass spectrometer with improved resolution. *Rev. Sci. Instrum.* **1955,** *26*, 1150-1157.

17. Baer, T.; Guyon, P. M.; Nenner, I.; Tabche-Fouhaille, A.; Botter, R.; Ferreira, L. F. A.; Govers, T. R. Non-Franck-Condon transitions in resonant autoionization of N_2O. *J. Chem. Phys.* **1979,** *70*, 1585-1592.

18. Guyon, P. M.; Baer, T.; Ferreira, L. F. A.; Nenner, I.; Tabche-Fouhaile, A.; Botter, R.; Govers, T. R. Observation of dissociative states of O_2^+ by threshold photoelectron photoion coincidence. *J. Phys. B:Atom. Molec. Phys.* **1978,** *11*, L141-L144.

19. Cole, S. K.; Baer, T.; Guyon, P. M.; Govers, T. R. Symmetric electron transfer reactions of state selected ions: $H_2^+(v) + H_2 \rightarrow H_2 + H_2^+(v=0\text{-}10)$. *Chem. Phys. Lett.* **1984,** *109*, 285-290.

20. Govers, T. R.; Guyon, P. M.; Baer, T.; Cole, K.; Frohlich, H.; Lavollee, M. State selected ion-molecule reactions: $N_2^+(X,v'')$, $N_2^+(A,v') + Ar \rightarrow N_2 + Ar^+$. *Chem. Phys.* **1984,** *87*, 373-387.

21. Richard-Viard, M.; Atabek, O.; Dutuit, O.; Guyon, P. M. Experimental evidence of vibrational mode selectivity in the indirect predissociation of oxodinitrogen(1+) (N2O+)A2S+. Energy distribution of the diatomic fragment and comparison with a model prediction. *J. Chem. Phys.* **1990,** *93*, 8881-8892.

22. Guyon, P. M.; Govers, T. R.; Baer, T. State selected ion-molecule reactions. *Z. Phys. D-Atoms,Molecules and Clusters* **1986,** *4*, 89-101.

23. Peatman, W. B.; Kasting, G. B.; Wilson, D. J. Origin and elimintion of spurious peaks in threshold electron photoionization spectra. *J. Electron Spectrosc. Relat. Phenom.* **1975,** *7*, 233-246.

24. King, G. C.; Zubek, M.; Rutter, P. M.; Read, F. H. A high resolution threshold electron spectrometer for use in photoionization studies. *J. Phys. E* **1987,** *20*, 440-443.

25. Avaldi, L.; Dawber, G.; Hall, R. I.; King, G. C.; McConkey, A. G.; MacDonald, M. A.; Stefani, G. Photoionization of acetylene near the threshold. *J. Electron Spectrosc. Relat. Phenom.* **1995,** *71*, 93-105.

26. Truong, S. Y.; Yencha, A. J.; Juarez, A. M.; Cavanagh, S. J.; Bolognesi, P.; King, G. C. Threshold photoelectron spectroscopy of H2O and D2O over the photon energy range 12-40eV. *Chem. Phys.* **2009,** *355*, 183-193.

27. Siggel-King, M. R. F.; Yencha, A. J.; King, G. C.; Malins, A. E. R.; Eypper, M. Formic and acetic acid: Valence threshold photoelectron and photoionisation total ion yield studies. *J. Electron Spectrosc. Relat. Phenom.* **2012,** *185*, 204-210.

28. Yencha, A. J.; Lopes, M. C. A.; King, G. C. Threshold photoelectron spectroscopy of iodine monochloride. *Chem. Phys. Lett.* **2000,** *325*, 559-567.

29. Hall, R. I.; McConkey, A.; Ellis, K.; Dawber, G.; Avaldi, L.; MacDonald, M. A.; King, G. C. A penetrating field electron-ion coincidence spectrometer for use in photoionization studies. *Meas. Sci. Technol.* **1992,** *3*, 316-324.

30. *SIMION 3D Version 8.1 is a software program that calculates ion or electron trajectories in static or time varying electric fields.,* Idaho National Engineering and Environmental Laboratory, Idaho Falls, ID 83415: 2012

31. Bolognesi, P.; King, G. C.; Avaldi, L. Photo-double-ionization of atoms. *Radiat. Phys. Chem.* **2004,** *70*, 207-236.

32. Hall, R. I.; Dawber, G.; McConkey, A. G.; MacDonald, M. A.; King, G. C. Threshold photoelectrons coincidence spectroscopy of the rare gases neon, argon, krypton, and xenon. *Zeitschrift fur Physikalische Chemie-International Journal of Research in Physical Chemistry & Chemical Physics* **1992,** *23*, 377-381.

33. Hall, R. I.; Dawber, G.; McConkey, A.; MacDonald, M. A.; King, G. C. Vibrational structure of the oxygen diatomic dipositive ion ground state observed by threshold photoelectron coincidence spectroscopy. *Phys. Rev. Lett.* **1992,** *68*, 2751-2754.

34. Hatherly, P. A.; Stankiewicz, M.; Codling, K.; Creasey, J. C.; Jones, H. M.; Tuckett, R. P. A threshold electron analyzer for use in coincidence experiments. *Meas. Sci. Technol.* **1992,** *3*, 891-896.

35. Smith, D. M.; Tuckett, R. P.; Yoxall, K. R.; Codling, K.; Hatherly, P. A.; Aarts, J. F. M.; Stankiewicz, M. Use of threshold electron and fluorescence coincidence techniques to probe the decay dynamics of the valence states of CF_4^+, SiF_4^+, $SiCl_4^+$, and $GeCl_4^+$. *J. Chem. Phys.* **1994,** *101*, 10559-10575.

36. Eppink, A. T. J. B.; Parker, D. H. Velocity map imaging of ions and electrons using electrostatic lenses: Application in photoelectron and photofragment ion imaging of molecular oxygen. *Rev. Sci. Instrum.* **1997,** *68*, 3477-3484.

37. Baer, T.; Li, Y. Threshold Photoelectron Spectroscopy with Velocity Focusing: An Ideal Match for Coincidence Studies. *Int. J. Mass Spectrom.* **2002,** *219*, 381-389.

38. Sztáray, B.; Baer, T. The suppression of hot electrons in threshold photoelectron photoion coincidence spectroscopy using velocity focusing optics. *Rev. Sci. Instrum.* **2003,** *74*, 3763-3768.

39. Garcia, G. A.; Soldi-Lose, H.; Nahon, L. A versatile electron-ion coincidence spectrometer for photoelectron momentum imaging and threshold spectroscopy on mass selected ions using synchrotron radiation. *Rev. Sci. Instrum.* **2009,** *80*, 023102-1-023102/12.

40. Johnson, P. M. Molecular Multiphoton Ionization Spectroscopy. *Acc. Chem. Res.* **1980,** *13*, 20-26.

41. Mueller-Dethlefs, K.; Sander, M.; Schlag, E. W. Two-color photoionization resonance spectroscopy of nitric oxide: complete separation of rotational levels of nitrosyl ion at the ionization threshold. *Chem. Phys. Lett.* **1984,** *112*, 291-294.

42. Mueller-Dethlefs, K.; Sander, M.; Schlag, E. W. A novel method capable of resolving rotational ionic states by the detection of threshold photoelectrons with a resolution of 1.2 cm-1. *Z. Naturforsch. A.* **1984,** *39*, 1089-1091.

43. Chewter, L. A.; Sander, M.; Mueller-Dethlefs, K.; Schlag, E. W. High resolution zero kinetic energy photoelectron spectroscopy of benzene and determination of the ionization potential. *J. Chem. Phys.* **1987,** *86*, 4737-4744.

44. Mueller-Dethlefs, K.; Schlag, E. W. High resolution zero kinetic energy (ZEKE) photoelectron spectroscopy of molecular systems. *Ann. Rev. Phys. Chem.* **1991,** *42*, 109-136.

45. Merkt, F. Collisional and electric field effects in the delayed pulsed field ionization zero-kinetic energy photoelectron spectrum of argon. *J. Chem. Phys.* **1994,** *100*, 2623-2628.

46. Merkt, F.; Fielding, H. H.; Softley, T. P. Electric field effects on zero kinetic energy photoelectron spectra: an explanation of observed trends. *Chem. Phys. Lett.* **1993,** *202*, 153-160.

47. Merkt, F.; Zare, R. N. On the lifetimes of Rydberg states probed by delayed pulsed field ionization. *J. Chem. Phys.* **1994,** *101*, 3495-3505.

48. Chupka, W. A. Factors affecting lifetimes and resolution of Rydberg states observed in zero-electron kinetic-energy spectroscopy. *J. Chem. Phys.* **1993,** *98*, 4520-4530.

49. Savee, J. D.; Zador, J.; Hemberger, P.; Sztaray, B.; Bodi, A.; Osborn, D. L. Threshold photoelectron spectrum of the benzyl radical. *Mol. Phys.* **2015,** *113*, 2217-2227.

50. Bodi, A.; Shuman, N. S.; Baer, T. On the ionization and dissociative photoionization of iodomethane: a definitive experimental enthalpy of formation of CH_3I. *Phys. Chem. Chem. Phys.* **2009,** *11*, 11013-11021.

51. Harvey, J.; Hemberger, P.; Bodi, A.; Tuckett, R. P. Vibrational and electronic excitations in fluorinated ethene cations from the ground up. *J. Chem. Phys.* **2013,** *138*, 124301-1-124301/11.

52. Johnson, P. M.; Zhu, L. Mass analyzed threshold ionization: structural information for a mass spectrum and mass information for ionic spectroscopy. *Int. J. Mass Spectrom. Ion. Proc.* **1994,** *131*, 193-209.

53. Bae, Y. J.; Kim, M. S. Photodissociation spectroscopy of CD_3I^+ generated by mass-analyzed threshold ionization for structure determination. *Chem. Phys. Chem.* **2008,** *9*, 1709-1714.

54. Bae, Y. J.; Kim, M. S. Rotational state selection of a CH3I + ion beam using vacuum ultraviolet-mass-analyzed threshold ionization spectroscopy: Characterization using photodissociation spectroscopy. *J. Chem. Phys.* **2008,** *128*, 124324-1-124324/7.

55. Weitzel, K. M.; Güthe, F. The distinction of direct and pulsed-field ionization zero kinetic energy photoelectrons in electron/ion coincidence experiments. *Chem. Phys. Lett.* **1996,** *251*, 295-300.

56. Jarvis, G. K.; Weitzel, K. M.; Malow, M.; Baer, T.; Song, Y.; Ng, C. Y. High resolution pulsed field ionization photoelectron photoion coincidence spectroscopy using synchrotron radiation. *Rev. Sci. Instrum.* **1999,** *70*, 3892-3906.

57. Weitzel, K. M.; Malow, M.; Jarvis, G. K.; Baer, T.; Song, Y.; Ng, C. Y. High-resolution pulsed field ionization photoelectron photoion coincidence study of CH_4: Accurate 0 K dissociation threshold for CH_3^+. *J. Chem. Phys.* **1999,** *111*, 8267-8270.

58. Jarvis, G. K.; Evans, M.; Ng, C. Y.; Mitsuke, K. Rotational-resolved pulsed field ionization photoelectron study of $NO^+(X\ ^1\Sigma^+, v^+=0\text{-}32)$ in the energy range of 9.24-16.80 eV. *J. Chem. Phys.* **1999,** *111*, 3058-3069.

59. Qian, X.-M.; Lau, K.-C.; Ng, C. Y. A high-resolution pulsed field ionization-photoelectron-photoion coincidence study of vinyl bromide. *J. Chem. Phys.* **2004,** *120*, 11031-11041.

60. Song, Y.; Ng, C. Y. Rotational-resolved pulsed field ionization -photoelectron study of NO^+ ($A^1\Sigma$-, v+ = 0-17) in the energy range of 17.70-20.10 eV. *J. Chem. Phys.* **2001,** *115*, 2101-2108.

61. Song, Y.; Evans, M.; Ng, C. Y.; Hsu, C. W.; Jarvis, G. K. Rotationally resolved pulsed field ionization photoelectron bands for $O_2^+(a\ ^4\Pi_u, v+=0\text{-}18)$ in the energy range of 16.0-18.0 eV. *J. Chem. Phys.* **2000,** *112*, 1306-1315.

62. Brehm, B.; Puttkamer, E. v. Coincidence measurement of photoproduced ions and electrons in methane. *Z. Naturforsch.* **1967,** *A22*, 8-10.

63. Eland, J. H. D. Photoelectron-photoion coincidence spectroscopy. I. Basic principles and theory. *Int. J. Mass Spectrom. Ion. Proc.* **1972,** *8*, 143-151.

64. Danby, C. J.; Eland, J. H. D. Photoelectron-photoion coincidence spectroscopy. II. Design and performance of a practical instrument. *Int. J. Mass Spectrom. Ion. Proc.* **1972,** *8*, 153-161.

65. Stockbauer, R. Threshold electron-photoion coincidence mass spectrometric study of CH_4, CD_4, C_2H_6, and C_2D_6. *J. Chem. Phys.* **1973,** *58*, 3800-3815.

66. Baer, T.; Guyon, P. M. Autoionization and isotope effect in the threshold photoelectron spectrum of $^{12}CO_2$ and $^{13}CO_2$. *J. Chem. Phys.* **1986,** *85*, 4765-4778.

67. Guyon, P. M.; Baer, T.; Nenner, I. Interactions between neutral dissociation and ionization continua in N_2O. *J. Chem. Phys.* **1983,** *78*, 3665-3672.

68. Merkt, F.; Guyon, P. M.; Hepburn, J. W. High resolution threshold photoelectron spectrum of molecular oxygen. *Chem. Phys.* **1993,** *173*, 479-489.

69. Holzmeier, F.; Lang, M.; Fischer, I.; Tang, X.; Cunha de Miranda, B.; Romanzin, C.; Alcaraz, C.; Hemberger, P. Threshold photoelectron spectroscopy of unstable N-containing compounds: Resolution of ΔK subbands in HNCO+ and vibrational resolution in NCO+. *J. Chem. Phys.* **2015,** *142*, 184306-18306/8.

70. Bodi, A.; Sztáray, B.; Baer, T.; Johnson, M.; Gerber, T. Data acquisition schemes for continuous two-particle time-of-flight coincidence experiments. *Rev. Sci. Instrum.* **2007,** *78*, 084102.

71. Franklin, J. L.; Hierl, P. M.; Whan, D. A. Measurement of the translational energy of ions with a time of flight mass spectrometer. *J. Chem. Phys.* **1967,** *47*, 3148-3153.

72. Baer, T.; Hase, W. L. *Unimolecular Reaction Dynamics: Theory and Experiments;* Oxford University Press: New York, 1996.

73. Boesl, U.; Neusser, H. J.; Weinkauf, R.; Schlag, E. W. Multiphoton mass spectrometry of metastables: Direct observation of decay in a high resolution TOF instrument. *J. Phys. Chem.* **1982,** *86*, 4857-4863.

74. Boesl, U.; Weinkauf, R.; Schlag, E. W. Reflectron time of flight mass spectrometry and laser excitation for the analysis of neutrals, ionized molecules and secondary fragments. *Int. J. Mass Spectrom. Ion. Proc.* **1992,** *112*, 121-166.

75. Mintz, D. M.; Baer, T. Kinetic energy release distributions for the dissociation of internal energy selected CH_3I^+ and CD_3I^+ ions. *J. Chem. Phys.* **1976,** *65*, 2407-2415.

76. Klots, C. E. Thermochemical and kinetic information from metastable decomposition of ions. *J. Chem. Phys.* **1973,** *58*, 5364-5367.

77. Tsai, B. P.; Werner, A. S.; Baer, T. A photoion photoelectron coincidence (PIPECO) study of fragmentation rates and kinetic energy release in energy selected metastable ions. *J. Chem. Phys.* **1975,** *63*, 4384-4392.

78. Baer, T.; Guerrero, A.; Davalos, J. Z.; Bodi, A. Dissociation of energy selected $Sn(CH_3)_4^+$, $Sn(CH_3)_3Cl^+$, and $Sn(CH_3)_3Br^+$ ions: Evidence for isolated excited state dynamics. *Phys. Chem. Chem. Phys.* **2011,** *13*, 17791-17801.

79. Creasey, J. C.; Jones, H. M.; Smith, D. M.; Tuckett, R. P.; Hatherly, P. A.; Codling, K.; Powis, I. Fragmentation of valence electronic states of CF_4^+ and SF_6^+ studied by threshold photoelectron-photoion coincidence spectroscopy. *Chem. Phys.* **1993,** *174*, 441-452.

80. Creasey, J. C.; Lambert, I. R.; Tuckett, R. P.; Codling, K.; Frasinski, L. J.; Hatherly, P. A.; Stankiewicz, M.; Holland, D. M. P. Nonradiative decay pathways of electronic states of group IV tetrafluoro and tetrachloro molecular ions studied with synchrotron radiation. *J. Chem. Phys.* **1990,** *93*, 3295-3306.

81. Hatherly, P. A.; Smith, D. M.; Tuckett, R. P. Nonstatistical effects in the fragmentation of electronic states of gas-phase polyatomic molecular ions. *Z. Phys. Chem.* **1996,** *195*, 97-136.

82. Dujardin, G.; Leach, S.; Dutuit, O.; Govers, T. R.; Guyon, P. M. Autoionization processes in symmetric trifluorobenzene and hexa-fluorobenzene: Studies involving threshold photoelectron spectroscopy and ion fluorescence. *J. Chem. Phys.* **1983,** *79*, 644-657.

83. Dujardin, G.; Leach, S.; Taieb, G. Fluorescence quantum yields and lifetimes of nine fluorobenzene cations. Electronic state relaxation processes. *Chem. Phys.* **1980,** *46*, 407-421.

84. Maier, J. P.; Thommen, F. Fluorescence quantum yields and lifetimes of fluorobenzene cations in selected levels of their B and C states determined by photoelectron-photon coincidence spectroscopy. *Chem. Phys.* **1981,** *57*, 319-332.

85. Schlag, E. W.; Frey, R.; Gotchev, B.; Peatman, W. B.; Pollak, H. Radiative lifetimes of ions from electron-photon coincidence measurements. *Chem. Phys. Lett.* **1977,** *51*, 406-408.

86. Chupka, W. A. Effect of unimolecular decay kinetics on the interpretation of appearance potentials. *J. Chem. Phys.* **1959,** *30*, 191-211.

87. Huang, F. S.; Dunbar, R. C. Time resolved photodissociation of methylnaphthalene ion. An illustration of kinetic shifts in large-ion dissociations. *J. Am. Chem. Soc.* **1990,** *112*, 8167-8169.

88. Lifshitz, C. Time-resolved appearance energies, breakdown graphs, and mass spectra: the elusive "kinetic shift". *Mass Spectrom. Rev.* **1982,** *1*, 309-348.

89. Bodi, A.; Kercher, J. P.; Baer, T.; Sztáray, B. On the Parallel Mechanism of the Dissociation of Energy-Selected P(CH3)3+ ions. *J. Phys. Chem. B* **2005,** *109*, 8393-8399.

90. Booze, J. A.; Weitzel, K. M.; Baer, T. The Rates of HCl Loss from Energy Selected Ethylchloride Ions: A case of Tunneling through an H-atom transfer Barrier. *J. Chem. Phys.* **1991,** *94*, 3649-3656.

91. Güthe, F.; Weitzel, K. M. Measurement of the rate constant k(E) of the unimolecular H_2 elimination from ethane radical cations in a reflectron mass spectrometer. *Ber. Bunsenges. Phys. Chem.* **1997,** *101*, 484-490.

92. Keister, J. W.; Baer, T.; Thissen, R.; Alcaraz, C.; Dutuit, O.; Audier, H.; Troude, V. Proton Tunneling in the Loss of Hydrogen Bromide from Energy-Selected Gas-Phase 2-Bromobutane Cations. *J. Phys. Chem. A* **1998,** *102*, 1090-1097.

93. Klots, C. E. Ionic Fragmentation through centrifugal barriers. *Chem. Phys. Lett.* **1971,** *10*, 422-423.

94. Li, Y.; Baer, T. Ethylene Glycol Ions Dissociate by Tunneling through an H-atom Transfer Barrier: A DFT and TPEPICO Study. *J. Phys. Chem. A* **2002,** *106*, 8658-8666.

95. Shuman, N. S.; Johnson, M.; Stevens, W. R.; Harding, M. E.; Stanton, J. F.; Baer, T. Tunneling in a simple bond scission: The surprising barrier in the H loss from $HCOOH^+$. *J. Phys. Chem. A* **2010,** *114*, 10016-10023.

96. Weitzel, K. M.; Mähnert, J. The direct measurement of the rate constant k(E) for the reaciton $C_2H_6^+ \rightarrow C_2H_4^+ + H_2$. *Z. Phys. Chem.* **1996,** *195*, 181-193.

97. Weitzel, K. M. Tunneling RRKM calculations for the H_2 loss reaction from ethane ions on an ab initio potential energy surface. *Int. J. Mass Spectrom. Ion. Proc.* **1994,** *136*, 1-24.

98. Bodi, A.; Brannock, M. D.; Sztáray, B.; Baer, T. Tunneling in H loss from energy selected ethanol ions. *Phys. Chem. Chem. Phys.* **2012,** *14*, 16047-16054.

99. Stevens, W.; Sztáray, B.; Shuman, N.; Baer, T.; Troe, J. Specific Rate Constants k(E) of the Dissociation of the Halobenzene Ions: Analysis by Statistical Unimolecular Rate Theories. *J. Phys. Chem. A* **2009,** *113*, 573-582.

100. Duffy, L. M.; Keister, J. W.; Baer, T. Isomerization and dissociation in competition: The pentene ion story. *J. Phys. Chem.* **1995,** *99*, 17862-17871.

101. Fischer, K. H.; Schneider, M.; Fischer, I.; Pfaffinger, B.; Braunschweig, H.; Sztáray, B.; Bodi, A. Bonding in a Borylene Complex Investigated by Photoionization and Dissociative Photoionization. *Chem. -Eur. Jour.* **2012,** *18*, 4533-4540.

102. Sztáray, B.; Bodi, A.; Baer, T. Modeling Unimolecular Reactions in Photoelectron Photoion Coincidence Experiments. *J. Mass Spectrom.* **2010,** *45*, 1233-1245.

103. Mayer, P. M.; Baer, T. A photoionization study of vibrational cooling in molecular beams. *Int. J. Mass Spectrom. Ion. Proc.* **1996,** *156*, 133-139.

104. Brechignac, Ph.; Garcia, G. A.; Falvo, C.; Joblin, C.; Kokkin, D.; Bonnamy, A.; Parneix, P.; Pino, T.; Pirali, O.; Mulas, G.; Nahon, L. Photoionization of cold gas phase coronene and its clusters: Autoionization resonances in monomer, dimer, and trimer and electronic structure of monomer cation. *J. Chem. Phys.* **2014,** *141*, 164325-1-164325/12.

105. Jacovella, U.; Holland, D. M. P.; Boye-Peronne, S.; Joyeux, D.; Archer, L. E.; de Oliveira, N.; Nahon, L.; Lucchese, R. R.; Xu, H.; Pratt, S. T. High-resolution photoabsorption spectrum of jet-cooled propyne. *J. Chem. Phys.* **2014,** *141*, 114303-1-114303/14.

106. Borkar, S.; Sztáray, B. Self-Consistent Heats of Formation for the Ethyl Cation, Ethyl Bromide, and Ethyl Iodide from Threshold Photoelectron Photoion Coincidence Spectroscopy. *J. Phys. Chem. A* **2010,** *114*, 6117-6123.

107. Booze, J. A.; Baer, T. On the determination of cluster properties by ionization techniques. *J. Chem. Phys.* **1992,** *96*, 5541-5543.

108. Booze, J. A.; Feinberg, T. N.; Keister, J. W.; Baer, T. The dissociative ionization of ethylene dimers, trimers, and tetramers studied by photoelectron photoion coincidence. *J. Chem. Phys.* **1994,** *100*, 4294-4299.

109. Nahon, L.; Garcia, G. A.; Harding, C. J.; Mikajlo, E. A.; Powis, I. Determination of chiral asymmetries in the valence photoionization of camphor enantiomers by photoelectron imaging using tunable circularly polarized light. *J. Chem. Phys.* **2006,** *125*, 114309.

110. Tang, X.; Garcia, G.; Gil, J. F.; Nahon, L. Vacuum upgrade and enhanced performances of the double imaging electron/ion coincidence end-station at the vacuum ultraviolet beamline DESIRS. *Rev. Sci. Instrum.* **2015,** *86*, 123108-1-123108/8.

111. Bodi, A.; Hemberger, P.; Gerber, T.; Sztáray, B. A new double imaging velocity focusing coincidence experiment: i2PEPICO. *Rev. Sci. Instrum.* **2012,** *83*, 083105-1-083105/8.

112. Garcia, G. A.; Cunha de Miranda, B. K.; Tia, M.; Daly, S.; Nahon, L. DELICIOUS III: A multipurpose double imaging particle coincidence spectrometer for gas phase vacuum ultraviolet photodynamics studies. *Rev. Sci. Instrum.* **2013,** *84*, 053112-1-053112/11.

113. Tang, X.; Zhou, X.; Niu, M.; Liu, S.; Sun, J.; Shan, X.; Liu, F.; Sheng, L. A threshold photoelectron - photoion coincidence spectrometer with double velocity imaging using synchrotron radiation. *Rev. Sci. Instrum.* **2009,** *80*, 113101-1-113101/10.

114. Baer, T.; Buchler, U.; Klots, C. E. Kinetic energy release distributions for the dissociation of internal energy selected $C_2H_5I^+$ ions. *J. Chim. Phys.* **1980,** *77*, 739-743.

115. Klots, C. E. Kinetic energy distributions from unimolecular decay: Predictions of the Langevin model. *J. Chem. Phys.* **1976,** *64*, 4269-4275.

116. Powis, I. The dissociation of state-selected CF_3X^+ molecular ions. *Mol. Phys.* **1980,** *39*, 311-327.

117. Tang, X.; Zhou, X.; Wu, M.; Gao, Z.; Liu, S.; Liu, F.; Shan, X.; Sheng, L. Dissociation limit and dissociation dynamic of CF4+: Application of threshold photoelectron-photoion coincidence velocity imaging. *J. Chem. Phys.* **2013,** *138*, 094306-1-094306/9.

118. Tang, X.; Zhou, X.; Niu, M.; Liu, S.; Sheng, L. Dissociation of Vibrational State-Selected O_2^+ Ions in the $B_2\Sigma_g^-$ State Using Threshold Photoelectron-Photoion Coincidence Velocity Imaging. *J. Phys. Chem. A* **2011,** *115*, 6339-6346.

119. Tang, X.; Zhou, X.; Wu, M.; Cai, Y.; Liu, S.; Sheng, L. Direct Experimental Evidence for Dissociative Photoionization of Oxygen Molecule via $^2\Sigma_u^-$ Ionic "Optical Dark" State. *J. Phys. Chem. A* **2012,** *116*, 9459-9465.

120. Tang, X.; Garcia, G. A.; Nahon, L. Adiabatic ionization energies of the overlapped A2A1 and B2E electronic states in CH3Cl+/CH3F+ measured with double imaging electron/ion coincidence. *Phys. Chem. Chem. Phys.* **2015,** *17*, 16858-16863.

121. Tang, X.; Lin, X.; Zhang, W.; Garcia, G. A.; Nahon, L. Double imaging photoelectron photoion coincidence sheds new light on the dissociation of energy-selected CH3Cl+ ions. *Phys. Chem. Chem. Phys.* **2016,** *18*, 23923-23931.

122. Osterwalder, A.; Nee, M. J.; Zhou, J.; Neumark, D. M. High resolution photodetachment spectroscopy of negative ions via slow photoelectron imaging. *J. Chem. Phys.* **2004,** *121*, 6317-6322.

123. Briant, M.; Poisson, L.; Hochlaf, M.; de Pujo, P.; Gaveau, M. A.; Soep, B. Ar_2 photoelectron spectroscopy mediated by autoionizing states. *Phys. Rev. Lett.* **2012,** *109*, 193401-1-193401/5.

124. Poully, J. C.; Schermann, J. P.; Nieuwjaer, N.; Lecomte, F.; Gregoire, G.; Desfrancois, C.; Garcia, G. A.; Nahon, L.; Nandi, D.; Poisson, L.; Hochlaf, M. Photoionization of 2-pyridone and 2-hydroxypyridine. *Phys. Chem. Chem. Phys.* **2010,** *12*, 3566-3572.

125. Garcia, G. A.; Nahon, L.; Powis, I. Two-dimensional charged particle image inversion using a polar basis function expansion. *Rev. Sci. Instrum.* **2004,** *75*, 4989-4996.

126. Dick, B. Inverting ion images without Abel inversion: maximum entropy reconstruction of velocity maps. *Phys. Chem. Chem. Phys.* **2014,** *16*, 570-580.

127. Dribinski, V.; Ossadtchi, A.; Mandelshtam, V. A.; Reisler, H. Reconstruction of Abel-transformable images: The Gaussian basis-set expansion Abel transform method. *Rev. Sci. Instrum.* **2002,** *73*, 2634-2642.

128. Gerber, T.; Liu, Y.; Knopp, G.; Hemberger, P.; Bodi, A.; Radi, P.; Sych, Y. Charged particle velocity map image reconstruction with one-dimensional projections of spherical functions. *Rev. Sci. Instrum.* **2013,** *84*, 033101-1-033101/10.

129. Heck, A. J. R.; Chandler, D. W. Imaging techniques for the study of chemical reaction dynamics. *Ann. Rev. Phys. Chem.* **1995,** *46*, 335-372.

130. Bodi, A.; Hemberger, P. Imaging breakdown diagrams for bromobutyne isomers with photoelectron-photoion coincidence. *Phys. Chem. Chem. Phys.* **2014,** *16*, 505-515.

131. Felsmann, D.; Moshammer, K.; Krueger, J.; Lackner, A.; Brockhinke, A.; Kapser, T.; Bierkandt, T.; Akyildiz, E.; Hansen, N.; Lucassen, A.; Osswald, P.; Koehler, M.; Garcia, G. A.; Nahon, L.; Hemberger, P.; Bodi, A.; Gerber, T.; Kohse-Hoeinghaus, K. Electron ionization, photoionization and photelectron/photoion coincidence spectroscopy in mass-spectrometry investigations of a low-pressure ethylen/oxygen flame. *Proc. Combust. Inst.* **2015,** *35*, 779-786.

132. Hansen, N.; Li, W.; Law, M. E.; Kasper, T.; Westmoreland, P. R.; Yang, B.; Cool, T. A.; Lucassen, A. The importance of fuel dissociation and propargyl + allyl association for the formation of benzene in a fuel-rich 1-hexene flame. *Phys. Chem. Chem. Phys.* **2010,** *12*, 12112-12122.

133. Moshammer, K.; Jasper, A. W.; Popolan-Vaida, D. M.; Lucassen, A.; Dievart, P.; Selim, H.; Eskola, A. J.; Taatjes, C. A.; Leone, S. R.; Sarathy, S. M.; Ju, Y.; Dagaut, P.; Kohse-Hoeinghaus, K.; Hansen, N. Detection and Identification of the Keto-Hydroperoxide (HOOCH2OCHO) and Other Intermediates during Low-Temperature Oxidation of Dimethyl Ether. *J. Phys. Chem. A* **2015,** *119*, 7361-7374.

134. Bodi, A.; Hemberger, P.; Osborn, D. L.; Sztáray, B. Mass-Resolved Isomer-Selective Chemical Analysis with Imaging Photoelectron Photoion Coincidence Spectroscopy. *J. Phys. Chem. Lett.* **2013,** *4*, 2948-2952.

135. Osswald, P.; Hemberger, P.; Bierkandt, T.; Akyildiz, E.; Koehler, M.; Bodi, A.; Gerber, T.; Kasper, T. In situ flame chemistry tracing by imaging photoelectron photoion coincidence spectroscopy. *Rev. Sci. Instrum.* **2014,** *85*, 025101-1-025101/11.

136. Felsmann, D.; Lucassen, A.; Krueger, J.; Hemken, C.; Tran, L. S.; Pieper, J.; Garcia, G. A.; Brockhinke, A.; Nahon, L.; Kohse-Hoeinghaus, K. Progress in Fixed-Photon-Energy Time-Efficient Double Imaging Photoelectron/Photoion Coincidence Measurements in Quantitative Flame Analysis. *Z. Phys. Chem.* **2016,** *230*, 1067-1097.

137. Krueger, J.; Garcia, G.; Felsmann, D.; Moshammer, K.; Lackner, A.; Brockhinke, A.; Nahon, L.; Kohse-Hoeinghaus, K. Photoelectron-photoion coincidence spectroscopy for multiplexed detection of intermediate species in a flame. *Phys. Chem. Chem. Phys.* **2014,** *16*, 22791-22804.

138. Osborn, D. L.; Hayden, C. C.; Hemberger, P.; Bodi, A.; Voronova, K.; Sztáray, B. Breaking Through the False Coincidence Barrier in Electron-Ion Coincidence Experiments . *J. Chem. Phys.* **2016,** *145*, 164202-1-164202-8.

139. Furuya, K.; Kimura, K. Energy partitioning in the dissociation reaction Ar_3^+-->Ar_2^+ + Ar. *J. Chem. Phys.* **1992,** *97*, 1022-1027.

140. Ruscic, B.; Pinzon, R. E.; Morton, M. L.; Laszevski, G.; Bittner, S. J.; Nijsure, S. G.; Amin, K. A.; Minkoff, M.; Leahy, D.; Montoya, D.; Wagner, A. F. Active Thermochemical Tables: thermochemistry for the 21st century. *J. Phys. Conf. Ser.* **2005,** *16*, 561-570.

141. Stevens, W. R.; Ruscic, B.; Baer, T. The heats of formation of C_6H_5, $C_6H_5^+$, and C_6H_5NO by TPEPICO and Active Thermochemical Tables analysis. *J. Phys. Chem. A* **2010,** *114*, 13134-13145.

142. Simpson, M. J.; Tuckett, R. P. Vacuum-UV negative photoion spectroscopy of gas-phase polyatomic molecules. *Int. Rev. Phys. Chem.* **2011,** *30*, 197-273.

143. Suits, A. G.; Hepburn, J. W. Ion pair dissociation: spectroscopy and dynamics. *Ann. Rev. Phys. Chem.* **2006,** *57*, 431-465.

144. Strahlman, C.; Sankari, R.; Nyholm, R.; Kivimaki, A.; Richter, R.; Coreno, M. A tandem time-of-flight spectrometer for negative-ion/positive-ion coincidence measurements with soft x-ray excitation. *Rev. Sci. Instrum.* **2016,** *87*, 013109.